DRUG DELIVERY
2025, VOL. 32, NO. 1, 2465909
https://doi.org/10.1080/10717544.2025.2465909

Taylor & Francis
Taylor & Francis Group

RESEARCH ARTICLE

OPEN ACCESS Check for updates

Machine learning-assisted design of immunomodulatory lipid nanoparticles for delivery of mRNA to repolarize hyperactivated microglia

Mehrnoosh Rafiei[a,b], Akbar Shojaei[b,c] and Ying Chau[a]

[a]Department of Chemical and Biological Engineering, The Hong Kong University of Science and Technology, Hong Kong, China; [b]Center for Nanoscience and Nanotechnology, Sharif University of Technology, Tehran, Iran; [c]Department of Chemical and Petroleum Engineering, Sharif University of Technology, Tehran, Iran

ABSTRACT

Regulating inflammatory microglia presents a promising strategy for treating neurodegenerative and autoimmune disorders, yet effective therapeutic agents delivery to these cells remains a challenge. This study investigates modified lipid nanoparticles (LNP) for mRNA delivery to hyperactivated microglia, particularly those with pro-inflammatory characteristics, utilizing supervised machine learning (ML) classifiers. We developed and screened a library of 216 LNP formulations with varying lipid compositions, N/P ratios, and hyaluronic acid (HA) modifications. The transfection efficiency of eGFP mRNA was assessed in the BV-2 murine microglia cell line under different immunological states, including resting and activated conditions (LPS-activated and IL4/IL13-activated). ML-guided morphometric analysis tracked the phenotypes of various microglia subtypes before and after transfection. Four supervised ML classifiers were investigated to predict transfection efficiency and phenotypic changes based on LNP design parameters. The Multi-Layer Perceptron (MLP) neural network emerged as the best-performing model, achieving weighted F1-scores ≥0.8. While it accurately predicted responses from LPS-activated and resting cells, it struggled with IL4/IL13-activated cells. The MLP model was validated by predicting the performance of four unseen LNP formulations delivering eGFP mRNA to LPS-activated BV2 cells. HA-LNP2 emerged as optimal formulation for delivering target IL10 mRNA, effectively suppressing inflammatory phenotypes, evidenced by shifts in cell morphology, increased IL10 expression, and reduced TNF-α levels. We also evaluated HA-LNP2 on LPS-activated human iPSC-derived microglia, confirming its efficacy in modulating inflammatory responses. This study highlights the potential of tailored LNP design and ML techniques to enhance mRNA therapy for neuroinflammatory disorders by leveraging carrier's immunogenic properties to modulate microglial responses.

GRACHICAL ABSTRACT

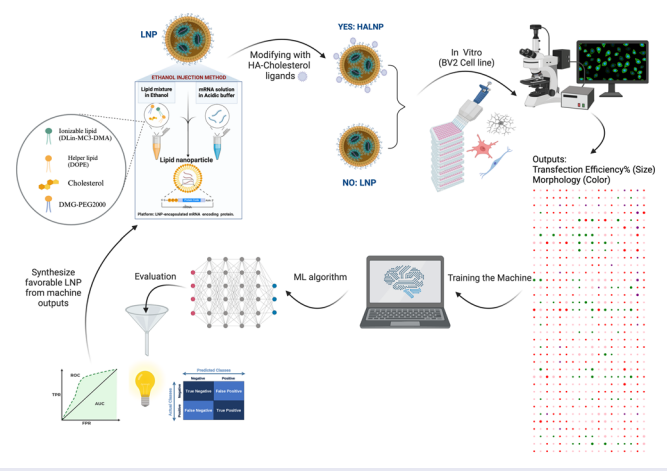

ARTICLE HISTORY

Received 9 October 2024
Revised 5 February 2025
Accepted 5 February 2025

KEYWORDS

Machine learning assisted; mRNA/LNP library; HA modification; microglia immunomodulation

CONTACT Ying Chau keychau@ust.hk Department of Chemical and Biological Engineering, The Hong Kong University of Science and Technology, Hong Kong, China

Supplemental data for this article can be accessed online at https://doi.org/10.1080/10717544.2025.2465909.

Introduction

The field of messenger RNA (mRNA) delivery using lipid nanoparticles (LNPs) is revolutionizing therapeutic approaches, particularly for immunomodulation (Hou et al., 2021; Rohner et al., 2022; Shi et al., 2022; Shimosakai et al., 2022). This groundbreaking technology has shown significant promise, highlighted by the successful development of mRNA vaccines for COVID-19 (Barbier et al., 2022; Rohner et al., 2022). Recent advancements have led to the creation of carriers designed for tissue-specific targeting, enhancing the delivery of mRNA to intended tissues while overcoming obstacles like degradation, clearance, and off-target effects (Wang et al., 2023). By prioritizing tissue/cell-specific targeting, researchers have made considerable progress in increasing the efficacy and safety of mRNA therapies (Veiga et al., 2018; Tanaka et al., 2021; Wang et al., 2023). However, to further propel this field, it is essential to investigate how these carriers influence various cell subtypes. Notably, manipulating the immunological phenotypes of microglia in the central nervous system (including the brain and the retina) represents a promising therapeutic strategy not only for glioblastoma but also for neurodegenerative diseases and ocular inflammation (Zhao et al., 2020; Kuntzel & Bagnard, 2022; Wang & Cepko, 2022; Sun et al., 2023).

Therapeutic mRNA administration holds significant potential for immunotherapeutic applications, offering advantages over traditional protein-based treatments (Jarzebska et al., 2021; Rohner et al., 2022; Shi et al., 2022; Yavuz et al., 2023). These include precise delivery of therapeutic molecules, reduced mutation risks through cytosolic translation, and the possibility of sustained expression of therapeutic proteins (Rohner et al., 2022). Despite these benefits, mRNA faces challenges such as instability and immunogenicity, which can be mitigated through effective delivery systems that protect the mRNA and sequence modifications to reduce immune responses (Hou et al., 2021; Riley et al., 2021; Shi et al., 2022; Zhang et al., 2022). LNPs have emerged as a promising solution for mRNA delivery, providing protection against degradation, enhancing cellular uptake, and improving transfection efficiency (Hou et al., 2021; Rohner et al., 2022). These properties have led to their clinical approval and widespread application in mRNA-based therapeutics (Han et al., 2021; Hou et al., 2021). However, the application of LNPs and other transfection reagents in immune cell studies requires careful consideration of their potential confounding effects on cellular responses. For instance, Lipofectamine MMAX, a widely used commercial transfection reagent, has been shown to induce type I interferon signaling in macrophages, which could potentially alter experimental outcomes and interpretations (Guo et al., 2019). This underscores the importance of characterizing the cellular response to any transfection reagent used in immune cell studies, including LNPs.

Microglia, the immune cells of the CNS and retina, are particularly important in this context (Choi et al., 2021; Qin et al., 2023). These highly plastic and dynamic cells can switch between different activation states in response to various stimuli (Cherry et al., 2014; Paolicelli et al., 2022; Reddaway et al., 2023). This adaptability is vital for their functions, including immune surveillance, tissue repair, and neuroprotection. Abnormal activation of microglial in the CNS leads to a pro-inflammatory state (Guo et al., 2022). This condition is characterized by the secretion of pro-inflammatory cytokines, such as TNF-α, IL-1β, and IL-6, which contribute to the malfunction and degeneration of brain neurons or retinal ganglion cells (RGCs). In contrast, anti-inflammatory microglia (rod subtype) support tissue healing and protection by releasing anti-inflammatory cytokines such as IL-10 and TGF-β (Au and Ma, 2017; Zhao et al., 2020; Choi et al., 2021; Guo et al., 2022). Pro-inflammatory-activation of microglia can lead to neurodegenerative diseases and ocular disorders, including uveitis, glaucoma, diabetic retinopathy, Alzheimer's disease, Parkinson's disease, and multiple sclerosis (MS) (Choi et al., 2021; Fan et al., 2022; Gao et al., 2023), and may also contribute to glioblastoma progression (Kuntzel & Bagnard, 2022; Sun et al., 2023).

By steering microglial polarization toward an anti-inflammatory phenotype, it is possible to mitigate inflammation, enhance neuronal and RGC survival, and slow disease progression (Cherry et al., 2014; Xiao et al., 2021; Wang & Cepko, 2022). Researchers may apply this strategy to produce more accurate and effective mRNA treatments for neuroinflammatory and ocular disorders. This approach requires a deeper understanding of the effects of mRNA carriers on different microglial activation states and the development of strategies to selectively modulate these cells. Traditionally, microglial activation has been simplified by researchers into two categories: pro-inflammatory (M1) and anti-inflammatory (M2) (Michelucci et al., 2009; Orihuela et al., 2016; Zhao et al., 2020). However, recent studies have revealed a complex spectrum of functional states, emphasizing the need for a nuanced understanding of microglial function in neuroinflammatory diseases (Li et al., 2022; Paolicelli et al., 2022; Reddaway et al., 2023). This complexity arises from the intricate interplay between environmental cues and signaling pathways that influence microglial polarization (Levi et al., 1998; Ginhoux et al., 2013; Karlstetter et al., 2015; Zhao et al., 2020; Qin et al., 2023).

For consistency and clarity, we will employ the standardized nomenclature proposed by Paolicelli et al. (2022) and Reddaway et al. (2023), which categorizes microglia into four distinct functional shapes: homeostatic (resting), rod, reactive, and amoeboid. This morphological classification is based on the soma size, processes appearance, and branching patterns of microglia. In a healthy CNS and retina, microglia typically exist in a surveillance and resting state, characterized by a ramified morphology with a small soma and thin, and highly branched processes (Qin et al., 2023). Upon stimulation, the stimuli signaling pathway triggers a response, directing microglia to transition into either a reactive state (pro-inflammatory subtype), characterized by an irregular body shape, enlarged soma and thicker processes, or a rod state (anti-inflammatory subtype), marked by a thin soma and long, polarized processes, or a combination of both. When the microglia reach their fully pro-inflammatory-activated state, it is known as the amoeboid state, characterized by a large soma and the absence or few number of processes (Giordano et al., 2021; Choi et al., 2022; Paolicelli et al., 2022; Reddaway et al., 2023). During neuroinflammation, the reactive microglia

retract their processes and adopt a rounded, amoeboid shape (Karunia et al., 2021; Martinez et al., 2023). After an injury, rod-shaped microglia align parallel to the damaged neurons, facilitating healing or degradation. This shift in morphology highlights the adaptability of microglia in response to their microenvironment (Au and Ma, 2017; Karunia et al., 2021).

Recent advancements in supervised Machine Learning (ML) have accelerated the optimization of mRNA/LNP formulations (Yamankurt et al., 2019; Ding et al., 2023; Ortiz-Perez et al., 2024). ML algorithms, such as Support Vector Machines (SVM), Random Forest (RF) Classifiers, Naïve Bayes classifiers, and Multi-Layer Perceptron (MLP) neural networks, have been employed to analyze complex datasets and predict the performance of various LNP formulations. These models can identify patterns and correlations that might not be evident through traditional analysis methods. By integrating ML algorithms with experimental data, researchers can more effectively engineer formulations to enhance the specificity and transfection of mRNA delivery systems.

This study aims to optimize LNP formulations for mRNA delivery to different subtypes of microglia and reveal how the carriers influence the immunological states of microglia, intending to repolarize the cells from pro-inflammatory to anti-inflammatory states while also maintaining their anti-inflammatory states during chronic inflammatory conditions. To comprehensively evaluate the LNP designs, we adopted a design of experiment (DOE) approach to create a diverse library of LNPs. This involved varying parameters such as the composition of lipids, molar ratios of chargeable groups in ionizable lipid to phosphate groups in mRNA (N/P ratio), and modification with hyaluronic acid (HA). HA is introduced as a design parameter because of its high affinity for CD44, a cell surface receptor that is upregulated in activated microglia and macrophages (Matsumoto et al., 2012; Hayward et al., 2016; Gao et al., 2023). Additionally, the innate immunosuppressive properties of HA and its similarity to the extracellular matrix (ECM) may render desirable cellular response (Buckley et al., 2022; Rafiei et al., 2023). While loaded with eGFP reporter mRNA, LNPs underwent high-throughput screening for transfection efficiency and impact on microglial phenotypic changes. In vitro experiments were performed in BV2, a well-established murine cell line for studying microglial functions (Yan et al., 2021). These cells were stimulated with either LPS or IL4/IL13 to generate pro-inflammatory and anti-inflammatory states, respectively (Yan et al., 2021; Kuntzel & Bagnard, 2022). The experimental data were utilized in training supervised multioutput ML classifier models, including SVM, RF Classifier, Naïve Bayes Gaussian Classifier, and MLP classifier. Through inlayer meticulous hyperparameter tuning and out-layer cross-validation, we were able to refine a predictive model capable of forecasting both transfection efficiency and cellular morphometric changes, based on specific LNP formulations for a particular microglia's initial state. A compelling application of this research was then demonstrated with the delivery of IL10-encoding mRNA to direct microglia transition from pro-inflammatory to anti-inflammatory phenotypes. The results highlight the potential of HA-LNPs as appropriate therapeutic mRNA carriers for treating inflammatory diseases.

This high-throughput screening of LNP design is the first to emphasize not only the transfection efficiency but also the immunomodulatory properties of the carriers. The significance of the results is elevated by focusing on microglia, whose immunological states are associated with the progression of a number of neuroinflammatory diseases. Thus, the cellular responses to exogenous nanocarriers cannot be overlooked. The novelty also arises from including in the LNP library the modification by HA, which imparts favorable features via the interaction with microglia. By leveraging ML for tracking the immunological states of microglia and for interpreting the data from screening experiments, we have demonstrated a feasible approach to increase the precision and effectiveness of mRNA therapies aimed at specific microglial activation states.

Materials and methods

Materials

The ionizable cationic lipid O-(Z,Z,Z,Z-heptatriaconta-6,9,26,29-tetraem-19-yl)-4-(N,N-dimethylamino) butanoate (DLin-MC3-DMA) was purchased from APExBIO (A8791, Houston, USA). The 1,2-distearoyl-sn-glycero-3-phosphocholine (DSPC), 1,2-dioleoyl-sn-glycero-3-phosphoethanolamine (DOPE), 1,2-dimyristoyl-rac-glycero-3-methoxypolyethylene glycol-2000 (DMG-PEG2000) were obtained from Avanti Polar Lipids (Al, USA). Cholesterol (Chol), Cholesteryl chloroformate, N-(3-Dimethylaminopropyl)-N′-ethylcarbodiimide Hydrochloride (EDC-HCL), Lipopolysaccharides from Escherichia coli O127:B8 (LPS), and Triton-X100 were obtained from Sigma–Aldrich (MO, USA). Recombinant Mouse IL-10 Protein (50245-MNAE), Recombinant Mouse IL-4 Protein (51084-MNAE), and Recombinant Mouse IL-13 Protein (50225-MNAH) were purchased from Sino Biological (Beijing, China). All culture dishes, TC treated (TCP011096) and CellATTACH treated (CAP011096) well plates, and confocal dishes were obtained from JetBioFil (GZ, China). For all experiments, TC-treated 96-well plates were utilized unless otherwise specified; in cases where CellATTACH-treated plates were used, this is explicitly stated. The polysaccharide Sodium hyaluronate MW ~36,000Da (HA (36 kDa)) was purchased from Bloomage Biotechnology (Shanghai, China). N-Hydroxysulfosuccinimide Sodium (Sulfo-NHS) was obtained from TCI America (Portland, USA). Phosphotungstic acid hydrate (PTA) was purchased from Biosynth (Beijing, China). Nuclease-Free Water and Lipofectamine MessengerMAX (Lipofectamine MMAX) Transfection Reagent was obtained from ThermoFisher Scientific (MA, USA).

Design and synthesis of mRNA and primers

EZ Cap eGFP mRNA (5-moUTP) (996 nucleotides) which was EZ capped modified with 5-Methoxyuridine-5′-Triphosphate was obtained from APExBIO (R1016, Houston, USA). Clean Cap Cy5 eGFP mRNA (5-moU) was obtained from TriLink Biotechnologies (L7701, CA, USA). IL10 mRNA (798 nucleotides based on NM_010548.2 with ORF shown in Table S1) modified with N1-Methyl-Pseudo-U Capped (Cap1) using CleanCap AG and Polyadenylated (120 A) was custom synthesized by TriLink Biotechnologies (CA, USA). All mRNA

structures in this study are modified with appropriate caps (5-moUTP, 5-moU, and Cap1) to avoid immune activation by the mRNA.

Cells

The murine microglial cell line BV2 (RRID: CVCL_0182) was kindly provided by Professor Karl W. K. Tsim and Professor Nancy Y. Ip's laboratory from the Hong Kong University of Science and Technology. This cell line was originally purchased from PUMC (1101MOU-PUMC000063, Peking, China). Murine macrophage RAW-Blue cell line (raw-sp, RRID: CVCL_X594) was obtained from Invivogen (CA, USA). Both cell lines were cultured in Dulbecco's modified Eagle's medium (DMEM), supplemented with 10% (v/v) heat-inactivated fetal bovine serum (HI FBS) and 1% (v/v) penicillin/streptomycin (10,000 units and 10,000µg/ml) in a humidified atmosphere with 5% CO2 at 37 °C. The subculture was performed every 2 to 3 days, ensuring that the cells reached a confluency of approximately 80% before passaging.

Human iPSC-derived microglia (iMG)

Frozen commercialized human induced pluripotent stem cell (iPSC)-derived microglia (iMG) were obtained from Axol (Male, ax0664, RRID: CVCL_E5SW). The cells were thawed and cultured at 37 °C with 5% CO_2 in a humidified incubator, following the manufacturer's recommendations. The thawed cells were first plated in a CellATTACH-treated 96-well plates at a density of 33,000 cells per well. After 24 h, a complete medium change was performed. Subsequently, half-medium changes were conducted every other day using the proprietary complete medium from Axol (ax0679). One day prior to transfection on day 7 after thawing, the cells were treated with LPS at a concentration of 100 ng/ml overnight. The following day, the medium was replaced with Opti-MEM, and transfection was carried out for 24 h. Following this time frame, the cytotoxity of the transfecting materials was determined using the MTT test.

LNP preparation and characterization

A mixture of lipids, including FDA-approved lipid formulations of ionizable lipid (Dlin-MC3-DMA), DOPE or DSPC, cholesterol, and DMG-PEG2000, were used in combination with mRNA aqueous phase to prepare LNPs via ethanol injection mixing method as previously described with some modifications (Chen et al., 2012; Kularatne et al., 2022; Wang et al., 2023). Dlin-MC3-DMA, DOPE or DSPC, cholesterol, and DMG-PEG-2000 were combined at different molar ratios as shown in Table 1 with a final lipid concentration of 12.5 mM as lipid stocks in ethanol. The aqueous phase contains eGFP mRNA or IL10 mRNA dissolved in 10 mM citrate buffer and different N/P ratios from 4 to 20 were used to prepare the LNPs. The ethanol and aqueous phases were mixed at a 1:3 ethanol:citrate volume ratio (Sayers et al., 2019; Wang et al., 2023). After 15 min of desiccation at room temperature to remove the ethanol, the LNPs were compensated with Phosphate-buffered saline (PBS) 1X, pH 7.4 buffer to a final volume of 10 µl for 96 well plate experiments (Roces et al., 2020). Before adding the complexes into the cell culture, the mixtures were incubated at room temperature for 20 minutes. A mRNA/Lipofectamine MMax complex (LipoPlex) was prepared according to the manufacturer's protocol with lipid to mRNA ratio optimized to 3 for BV2 cells.

Table 1. The range of parameters for LNP formulations.

Parameter	Parameter values
MC3 + DOPE %	40, 60, 80
MC3/DOPE	1, 2, 5, 10
DMG-PEG2000%	0, 0.5, 1.5
N/P ratio	4, 8, 12
HA modification	Yes, No

The particle size, polydispersity index (PDI), and zeta potential were measured by dynamic light scattering (DLS) (NanoBrook ZetaPlus zeta potential analyzer, Brookhaven Instruments Ltd, Holtsville, NY, USA). Freshly made LNPs were diluted 1:100 in deionized water in cuvettes for measurement by a DLS device. For transmission electron microscopy (TEM), the carbon-coated 400 mesh copper grid was first plasma-treated for 1mins to enhance the LNP attachment. Three microliters of freshly prepared LNP were then deposited on the grid for 1 mins and blotted with wet filter paper. Subsequently, three microliters of filtered deionized (DI) water were applied to the grid for 5 s and then blotted. Three microliters of negative staining, and 1% PTA was added to the grid for 10 seconds. The solution was carefully removed using wet filter paper, and the grid was dried under vacuum overnight. The copper grid containing LNP samples was examined by transmission electron microscopy (TEM) (JEM 2010F; JEOL, Tokyo, Japan). Scanning electron microscopy (SEM) with a field emission microscope (JSM-6700F SEM, JEOL, Tokyo, Japan) operating at an acceleration voltage of 5.0 kV was also used to characterize the morphology of LNPs. To prepare the samples, they were diluted with water to achieve a solid content of approximately 0.01%. The diluted samples were then drop-cast onto a silicon wafer for analysis. The mRNA encapsulation efficiency was determined using Quant-it RiboGreen assay (Invitrogen, USA) following the manufacturer's protocol. Briefly, LNPs were diluted 1:100 to 1:400 in 1× TE buffer in two microcentrifuge tubes per LNP formulation. 2% v/v Triton X-100 was added to one of the tubes and both were heated to 37 °C and gently shaken for 5 min, followed by cooling to room temperature for 10 min. LNP samples and RNA standards were plated in triplicate in black 96-well plates and the fluorescent reagent was added based on the manufacturer's instructions. Fluorescent intensity was read with a Varioskan LUX multimode microplate reader (Thermo Scientific, USA) (excitation, 485 nm; emission, 528 nm). RNA content was quantified by comparing samples to the mRNA standard curve, and encapsulation efficiency (EE%) was calculated according to the equation $EE\% = (B - A)/B \times 100$, where A is the RNA content in samples without Triton X-100 treatment (intact LNPs), and B is the RNA content in samples treated with Triton X-100 (lysed LNPs) (Young et al., 2024).

Modification of LNP with HA

Synthesis of HA-Chol ligands

HA-Chol (Cholesterol) ligands were prepared based on EDC/MHS synthesis route as shown in Fig. S1 (Pan et al., 2016).

In brief, anhydrous ethylenediamine (0.67 mmol/ml) and triethylamine (TEA) (300 µL) were dissolved in anhydrous dichloromethane (DCM) (100 mL). Cholesteryl chloroformate (0.1 mmol/ml) in anhydrous DCM was added dropwise to this solution under nitrogen purging at 4 °C for 2 h. Following the addition, the mixture was stirred further overnight at room temperature. The solution was then filtered, washed with distilled water three times, dried over anhydrous magnesium sulfate, and vacuum dried. Afterward, the resulting residue was redissolved in DCM and precipitated in methanol (MeOH) at a 1:1 volume ratio. The precipitate was subsequently filtered and vacuum-dried, yielding a cholesteryl amine (Chol-Am) product with 100% DM (Xue et al., 2011; Pan et al., 2016). To chemically modify HA with Chol-Am, sodium hyaluronate with 36 kDa molecular weight (100 mg), EDC-HCL (50 mg), and sulfo-NHS (56 mg) were dissolved in distilled water:N, N-dimethylformamide (DMF) (1:3, v/v) containing 0.1 M phosphate buffer (PB) with pH = 6.5 and stirred in an ice bath for 2 h to activate the carboxyl group of HA. After activation, Chol-Am (7 mg) dissolved in DMF (10 mL) was added dropwise to the activated HA solution. After stirring overnight, the resulting precipitate was thoroughly washed with ethanol by precipitation in extra volume ethanol (EtOH) (5 times) by putting in RT for 3 h. Afterward, the precipitate redissolved in water:EtOH and dialyzed against deionized water for 72 h using a dialysis membrane with an MW cutoff (MWCO) of 3,500. The dialyzed solution was filtered and freeze-dried to obtain HA–Chol ligands. Degree of modification (DM) was the number of Chol molecules per 100 sugar residues of HA determined by 1H nuclear magnetic resonance (NMR). HA–Chol was dissolved in D_2O (deuterium oxide) and analyzed by ^{1}H-NMR (300 MHz) (Xue et al., 2011; Hayward et al., 2016; Pan et al., 2016).^{1}H-NMR spectroscopy of HA-Cholesterol ligand was reported in Fig. S1.

HA-LNP preparation using post-insertion

The post-insertion strategy was used similar to Swart et al. work (Swart et al., 2022) to add HA-Chol ligands to the pre-formed mRNA/LNP systems (Hu et al., 2016; Pan et al., 2016). In brief, after evaporation of ethanol, the HA-Chol ligands were added to the mRNA/LNP solution with different molar ratios of HA-Chol to lipids from 2% to 10%. The HA-LNPs were developed using a positive representative LNP, referred to as LNP2, with varying molar ratios of HA-Chol ligands to lipids set at 2%, 5%, and 10%. Our analysis, conducted through dynamic light scattering (DLS), encapsulation efficiency (EE%), and transfection efficiency, revealed that the 2% formulation achieved a high EE% of 78% ± 3, with over 80% of the cells exhibiting a positive green signal at this concentration, as detailed in Supplementary Table S2. Conversely, the 5% formulation retained an EE% above 70%, but its transfection efficiency fell below 80%. The 10% formulation demonstrated an EE% of less than 70%, along with a transfection efficiency also below 80%. We propose that the decline in transfection efficiency observed with increasing ligand concentrations can be attributed to two primary factors. First, the increased ionic strength resulting from the negative charge of HA may cause premature release of mRNA before transfection occurs. Second, the overall increase in the negative surface charge of the formulation may impede cellular uptake, making it less effective for cellular applications. Therefore, we have determined that the 2% HA modification is the optimal formulation for this study, and all references to HA modification throughout the manuscript specifically refer to this 2% concentration.

Cytotoxicity assay

Cells were seeded overnight in 96-well plates at a density of 15,000 cells per well to ensure optimal growth (80% confluency) and adherence. Following this, samples of mRNA/LNP or mRNA/HA-LNP were added to the cells at a concentration of 100–250ng of eGFP per 15,000 cells and incubated for 24 h at 37°C. After incubation, 10 µL of MTT (M6494, ThermoFisher, US) solution (12 mM) was added to each well and incubated for 4 hours at 37 °C. The supernatants were then removed, and 100 µL of DMSO was added to each well. The mixture was shaken for 10 min at room temperature. Finally, the absorbance was measured at 570 nm using a Varioskan LUX multimode microplate reader.

Immuno-stimulation of BV2

LPS, recombinant mouse IL-4, and recombinant mouse IL-13 were used to create different microglial phenotypes in vitro. For the proinflammatory phenotype, we used LPS at a concentration of 200 ng/ml. To induce an anti-inflammatory phenotype, we utilized a combination of IL-4 and IL-13 cytokines, each at a concentration of 25 ng/ml. Both treatments were applied overnight on BV2 (Yan et al., 2021). Immunocytochemistry was used to evaluate these phenotypes prior to transfection reagent treatment.

Immunocytochemistry of BV2

BV2 cells were incubated overnight in a confocal dish (Jet Biofil, Guangzhou, China) at a density of 100,000 cells per dish and were subjected to stimulation treatments as appropriate. Subsequently, the cells were fixed using 4% paraformaldehyde (PFA) in 1X PBS and washed with PBS. To permeabilize the cells, they were treated with 0.2% Triton-X 100 for 10 min and then incubated in 2% BSA in PBS for 1 h to prevent nonspecific binding. The primary antibody CD44 (clone IM7, RRID: AB_3662602, 39037) Rat mAb (1:400; Cell Signaling Technology, MA, USA) was applied to the BV2 cells. For visualization, a secondary antibody, Goat Anti-rabbit IgG (Alexa Fluor® 594 Conjugate, RRID: AB_2716249, 8889) (1:1000; Cell Signaling Technology, MA, USA), was used alongside the nuclear stain 4,6-diamidino-2-phenylindole (DAPI) (1:1000; Sigma–Aldrich, MA, USA). Images were captured using an SP8 confocal laser scanning microscope (CLSM) from Leica Microsystems (Germany).

Quantitative reverse transcription-polymerase chain reaction (qRT-PCR)

Total RNA was extracted from the non-stimulated and stimulated BV2 cell line after 16 hours post-stimulation or seeding using RNeasy Mini Kit (Qiagen, Hilden, Germany) and

following the manufacturer's protocol. RNA quantity was assessed by a NanoDrop (ThermoFisher Scientific, MA, USA) UV/Vis spectrophotometer. The reagent TB green master mix was prepared with One-Step TB Green PrimeScript RT-PCR Kit II (Perfect Real Time) (TAKARA, Shiga, Japan) following the manufacturer's protocol. The quantitative reverse transcription-polymerase chain reaction (qRT-PCR) was performed on the LightCycler 480 system (Roche Diagnostic, CA, USA) with a 3-step PCR including 1 cycle reverse transcription (42 °C for 5 min, and 95 °C for 10 s), 40 cycles PCR reaction (95 °C for 5 s, 60 °C for 30 s, and 72 °C for 30 s) and melting curve analysis based on manufacturer's protocol. The primers used for the qRT-PCR were custom-synthesized by Life Technologies and included the following sequences: for Mouse β-Actin, the forward primer was GGCACCACACCTTCTACAATG, and the reverse primer was GGGGTGTTGAAGGTCTCAAAC; for Mouse CD206, the forward primer was CTTCGGGCCTTTGGAATAAT, and the reverse primer was TAGAAGAGCCCTTGGGTTGA; for Mouse CD86, the forward primer was ACGATGGACCCCAGATGCACCA, and the reverse primer was GCGTCTCCACGGAAACAGCA. Data were analyzed by the $2^{-\Delta\Delta C_t}$ method (Livak & Schmittgen, 2001) and normalized to those of microglia b-Actin. Then the relative gene expression values were calculated as a fold change in which the mean value of the control group (non-treated cells) was considered 1.

BV2 cellular uptake of LNP and HA-LNP using CD44 blocking assay

To investigate the role of the CD44 receptor in the cellular internalization of HA-LNPs, a receptor-blocking assay was conducted. BV2 cells were cultured overnight on a confocal dish with a number of 100,000 cells/dish. The following morning, a subset of wells received a pretreatment with HA (36 kDa) for 1 h at 37 °C. This pretreatment aimed to saturate the CD44 receptors, effectively blocking their availability for subsequent interactions. Following the pretreatment, HA-LNPs were added to all wells, containing Cy5 eGFP mRNA at a concentration of 1.8 µg/ml, and incubated for 4 hours. After incubation, cells were fixed and stained with DAPI and Flash Phalloidin same as the Immunocytochemistry protocol stated before. SP8 Confocal microscopy was employed to quantify the uptake of Cy5eGFP mRNA per cell in both HA-pretreated and non-HA-pretreated samples. Differences in fluorescence intensity between the two groups were analyzed to determine the contribution of CD44 receptor-mediated internalization to the overall uptake of HA-LNPs.

Transfection of BV2 using eGFP mRNA reporter

To verify the transfection ability of HA-LNPs and LNPs encapsulated with eGFP mRNA, transfection experiments were conducted on BV2 cells in vitro. BV2 cells were seeded in a 96-well plate at a density of 15,000 cells/well and were allowed to grow at 70% confluency overnight. The next day the cell's medium was switched to OptiMEM reduced serum (by at least 50%) medium and incubated at 37 °C 10 mins. Then 10 µl of freshly prepared eGFP mRNA/LNP or HA-LNP formulations were added to each well, with final mRNA concentrations varying from 1 ng/ul, 1.5 ng/ul to 2.5 ng/ul, and the cells were cultured in 100 µl OptiMEM. The cells were subsequently analyzed after 24 h of incubation using a fluorescent microscope with fixed gain and shutter for all groups in this study (ECLIPSE Ti2 inverted microscope, Nikon, USA). Both GFP+ and GFP- cells from bright field and fluorescent images were counted, and the mean fluorescent intensity was measured with ImageJ software. Transfection efficiency indicates the percentage of GFP+ cells. The workflow for analyzing the images is depicted in Fig. S2 (Left).

Morphometric studies of BV2 cells

To characterize the morphological changes in BV2 cells under different treatment conditions, we employed a comprehensive morphometric analysis using bright field (BF) microscopy and advanced image processing techniques. Our approach was adapted from the methodology described in previous works (Fernández-Arjona M del et al., 2019; Leyh et al., 2021; Martinez et al., 2023) with modifications to suit our specific experimental setup and analysis pipeline. One day after transfection, BF microscopy images of BV2 cells were captured using a fluorescent microscope (ECLIPSE Ti2 inverted microscope, Nikon, USA) at 20X magnification with at least three images from each well. These images were then processed and analyzed using AIVIA software (AIVIA13, Leica Microsystems, Germany), which employs ML-based object classification to categorize cells based on their morphological features. The workflow for analyzing the images obtained from the microscope using AIVIA is depicted in Fig. S2 (Right). The morphological classification was based on four distinct microglial phenotypes: homeostatic, rod, reactive, and amoeboid (Fernández-Arjona M del et al., 2019; Leyh et al., 2021; Choi et al., 2022). Each phenotype was defined by specific ranges of morphometric parameters: (Shi et al., 2022) Homeostatic: cell area 200–8,000µm^2, skeleton length 200–350 µm, and cell solidity 0.25–0.3; (Hou et al., 2021) Rod: cell area 300–700µm^2, skeleton length 200–350 µm, and cell solidity 0.25–0.3; (Shimosakai et al., 2022) Reactive: cell area 200–400µm^2, skeleton length 100–300 µm, and cell solidity 0.3–0.35; (Rohner et al., 2022) Amoeboid: cell area 50–150µm^2, skeleton length 25–50 µm, and cell solidity 0.4–0.5. For more details, the reader could refer to Martinez et al. work (Martinez et al., 2023). The AIVIA software's object classifier was trained on a subset of manually classified cells to recognize these distinct morphological features. Each region of interest (ROI) contained about 300 cells, with at least three ROIs analyzed per condition, leading to a total of approximately 1,000 cells per condition. This methodical approach enhances the robustness and reliability of morphological analyses across various experimental conditions. Following training, the classifier was applied to the entire dataset of cell images. For each image, the software analyzed individual cells and classified them into one of the four phenotypes based on their morphometric parameters. The output of this analysis provided the percentage of cells in each phenotype category for every image. It is important to note that each condition is a heterogeneous blend of all phenotypes. To identify the prevalent phenotype within each experimental condition, we reported the phenotype with the highest population percentage among the four categories. This approach allowed us

to quantitatively assess the morphological shifts in BV2 cells in response to various treatments and stimuli. This morphometric analysis provided crucial insights into the activation states of BV2 cells under different experimental conditions, allowing us to correlate morphological changes with functional alterations in our subsequent analysis.

Enzyme-linked immunosorbent assay (ELISA)

To assess the expression levels of IL10 and TNF-α in LPS-activated BV2 cells, mouse IL10 ELISA MAX Deluxe Set Mouse IL10 (431414, Biolegend, CA, USA) and ELISA MAX Deluxe Set Mouse TNF-α (430904, Biolegend, CA, USA) were used following the manufacturer's protocol. The IL-10 ELISA kit includes a mouse IL-10 standard, a mouse IL-10 capture antibody (200X), and a mouse IL-10 detection antibody (200X). Similarly, the TNF-α ELISA kit contains a mouse TNF-α standard, a mouse TNF-α capture antibody (200X), and a mouse TNF-α detection antibody (200X). This allowed for the measurement of IL10 and TNF-α expression in comparison to controls, which included unstimulated cells, LPS-activated cells, and cells stimulated with IL4/IL13. Additionally, cells treated with IL10 cytokine at a concentration of 100 ng/ml served as another control. For the transfection of IL10 mRNA, BV2 cells stimulated with LPS (seeded at 15,000 cells per well in a 96-well plate) were transfected using various carriers: LNP, HA-LNP, and Lipofectamine MMAX, each containing a final concentration of 1.4 µg/ml of IL10 mRNA. The experiment was conducted over 48 h post-transfection, with the medium collected every 24 h for ELISA analysis according to the manufacturer's guidelines and replaced with fresh medium. The concentrations in each well were determined by measuring absorbance at 450 nm using a Varioskan LUX multimode microplate reader.

RAW-blue assay

A 96-well plate was seeded with 10,000 RAW-Blue cells per well for 24 h. After removing the culture media, each well was treated with transfection reagents (mRNA/LNP, mRNA/HA-LNP, and mRNA/LipofectamineMMAX) containing various mRNA types, such as eGFP and IL10. After 24 h of cell treatment, the supernatant was collected. Using a QUANTI-Blue detection medium made according to the manufacturer's protocol, the NF-κB activation level was measured. After adding 20 µL of culture supernatant to 180 µL of QUANTI-Blue reagent mix (rep-qbs, InvivoGen, CA, USA), the mixture was incubated for two hours at 37 °C. The Varioskan LUX multimode microplate reader was used to detect absorbance at 620 nm in order to calculate the SEAP levels. A fresh culture medium without any cells served as the blank, while LPS-activated cells (100 ng/mL) and recombinant mouse IL10-activated cells (100 ng/mL) were used as controls.

Machine learning approach

We compiled a comprehensive dataset from our in vitro experiments, encompassing 216 LNP formulations with and without HA modifications, their synthesis properties, and the corresponding transfection efficiencies and morphological outcomes in BV2 microglia cells under different activation states. The input features included lipid composition ratios, N/P ratio, and HA modification. To ensure robust analysis, we aggregated data from three repeated measurements for each condition by calculating the mean cell transfection efficiency and cell morphology outputs. The standard deviation of these measurements was consistently found to be less than 10% of the mean values, indicating a narrow spread among the data points. This low level of variability allowed us to minimize noise and fluctuations, providing stable inputs for model training. The ML task that we employed was a multioutput classification task. The target variables were transfection efficiency label $\in$ (0, 1) (binary classification: 1 indicating sufficient >80%, and 0 indicating insufficient <80%), and post-transfection morphology was categorized according to a binary classification (Homeostatic|Rod vs. Reactive|Amoeboid) as representatives of anti-inflammatory and pro-inflammatory direction. When the morphometric analyses from AIVIA indicated that the combined percentage of Homeostatic and Rod categories exceeded 50%, the group was classified as Homeostatic|Rod. Conversely, if the combined percentage of Reactive and amoeboid categories surpassed 50%, the group was classified as Reactive|Amoeboid. We implemented four supervised multi-output classifier machine learning models using the scikit-learn library (Python 3.11.7): Random Forest Classifier (RF), Support Vector Machine (SVM), Multi-Layer Perceptron (MLP) Neural Network Classifier, and Naïve Bayes Gaussian Classifier. Each model was configured to simultaneously predict both transfection efficiency and post-transfection morphology. To ensure consistent performance across different algorithms, feature scaling was performed using "StandardScaler" to normalize the input features.

The dataset was randomly split into two subsets: 80% for training-validation and 20% hold-out for testing. This split facilitated both the training-validation of the models and the subsequent evaluation of their performance on unused data. Hyperparameter tuning was conducted using "RandomizedSearchCV" with a 5-fold stratified cross-validation to optimize model performance. We defined hyperparameter grids for each model. For the RF model, we tuned parameters such as the number of estimators (n_estimators), maximum depth (max_depth), minimum samples required to split an internal node (min_samples_split), and minimum samples required at a leaf node (min_samples_leaf). The Neural Network's (MLP) hyperparameters included the sizes of the hidden layers (hidden_layer_sizes), regularization strength (alpha), and learning rate options. The SVM model was optimized for the regularization parameter (C), kernel type, and gamma value. The Naive Bayes model did not require hyperparameter tuning due to its parameter-free nature. We employed a nested cross-validation approach with an outer 5-fold cross-validation loop and an inner 3-fold cross-validation loop for hyperparameter tuning. The outer cross-validation was implemented using "KFold", ensuring data shuffling for bias prevention and maintaining a consistent random state for reproducibility.

For each iteration of the outer cross-validation, the training-validation set was further split into training (70%) and validation (30%) subsets, facilitating the hyperparameter tuning on the training subset while using the validation subset to gauge the hyperparameters' performance.

Model performance was evaluated using the weighted F1 score (Takahashi et al., 2023), providing an assessment of

classification effectiveness. The weighted F1-score provides a balance between precision and recall, particularly useful in scenarios with imbalanced classes, ensuring that the performance reflects the model's ability to classify minority classes accurately and is defined as:

$$Weighted\ F1\ score = \frac{\sum_{i=1}^{N} \omega_i . F1_i}{\sum_{i=1}^{N} \omega_i}$$

where:

N is the number of classes that is 2 for each output here,

$F1_i$ is the F1-score for class i,

ω_i is the weight for class i, defined as the proportion of instances of class i in the dataset, as detailed in supplementary Table S3.

The F1-score for each class is calculated as:

$$F1_i = \frac{Precision_i . Recall_i}{Precision_i + Recall_i}$$

with Precision and Recall defined as:

$$Precision_i = \frac{TP_i}{TP_i + FP_i}$$

$$Recall_i = \frac{TP_i}{TP_i + FN_i}$$

where:

TP_i is the true positives for class i,

FP_i is the false positives for class i,

FN_i is the false negatives for class i.

Based on the cross-validation results and hyperparameter tuning, the best-performing models with the highest F1-score for transfection efficiency and morphology prediction were selected. These best models were then validated on the hold-out test set (20% of the data) to assess their prediction capability, checking whether our findings are robust and reliable for practical applications. After identifying the best models, we conducted further evaluations using advanced metrics and visualization techniques. The AUC-ROC (Area Under the Receiver Operating Characteristic Curve) is employed as a measure of the model's ability to distinguish between classes, with a higher AUC indicating better performance. This metric is valuable for assessing the model's effectiveness in transfection, as it accurately reflects the true positive rate (TPR). The AUC–ROC is derived by plotting the TPR against the false positive rate (FPR) across various threshold settings. The formula for calculating AUC is given by:

$$AUC = \int_0^1 TPR\left(FPR\right) dFPR$$

Where:

$$TPR = \frac{TP}{TP + FN}\left(True\ Positive\ Rate\ same\ as\ Recall\right)$$

$$FPR = \frac{FP}{FP + TN}\left(False\ Positive\ Rate\right)$$

The AUC value ranges from 0 to 1, with 1 indicating perfect discrimination between classes and 0.5 indicating no discrimination. For the morphology prediction task, we created confusion matrices to visualize the classification performance of the models. Furthermore, we performed SHAP (SHapley Additive exPlanations) analysis using the SHAP Python library to examine the impact of individual features on model predictions and outputs for the best-performing models in transfection efficiency and morphology prediction. We generated SHAP summary beeswarm plots, mean absolute SHAP value plots, and waterfall plots to illustrate the distribution of SHAP values, average feature importance, and individual feature contributions for each instance, respectively.

In this study, we employed mean contribution ranking to assess the importance of features in our experimental data for transfection efficiency and cell morphology. To ensure comparability and mitigate the effects of differing scales, we normalized the feature values using min-max normalization, which rescales each feature to a range between 0 and 1. The mean of these normalized values was then calculated for each feature, providing a central measure of their contributions. This approach allowed us to effectively rank the features and compare them with the rankings derived from mean absolute SHAP values.

Statistical analysis

Numerical data are expressed as mean ± standard deviation (s.d.), $n = 3$. Each experiment was conducted in triplicate. Statistical analyses were conducted using two-way analysis of variance (ANOVA) accompanied by Tukey's multiple comparison tests within GraphPad Prism 10 software. This approach enabled comparisons between each treatment group and their respective control groups. Statistical significance was determined at $p < 0.05$, with the following thresholds for significance: **** for $p < 0.0001$, *** for $p < 0.0002$, ** for $p < 0.0021$, and * for $p < 0.0332$.

Results and discussion

LNP library synthesis and physiochemical characterization

The LNP formulations in our library were composed of DLin-MC3-DMA as ionizable lipid, DOPE as neutral helper lipids, DMG-PEG2000 as PEGylated lipid, cholesterol and HA modification (Figure 1(A)). The synthesis of HA-Chol ligands was successfully achieved, resulting in a 30% degree of substitution (DS), which reflects the conjugation efficiency of cholesteryl-ethylenediamine to HA. This was confirmed through ^{1}H-NMR spectroscopy (Fig. S1). Following the synthesis, the pre-formed mRNA/LNP systems were modified using the HA-Chol ligands. To verify the successful modification of the LNPs with HA, we analyzed the size and zeta potential before and after the modification. Additionally, TEM and

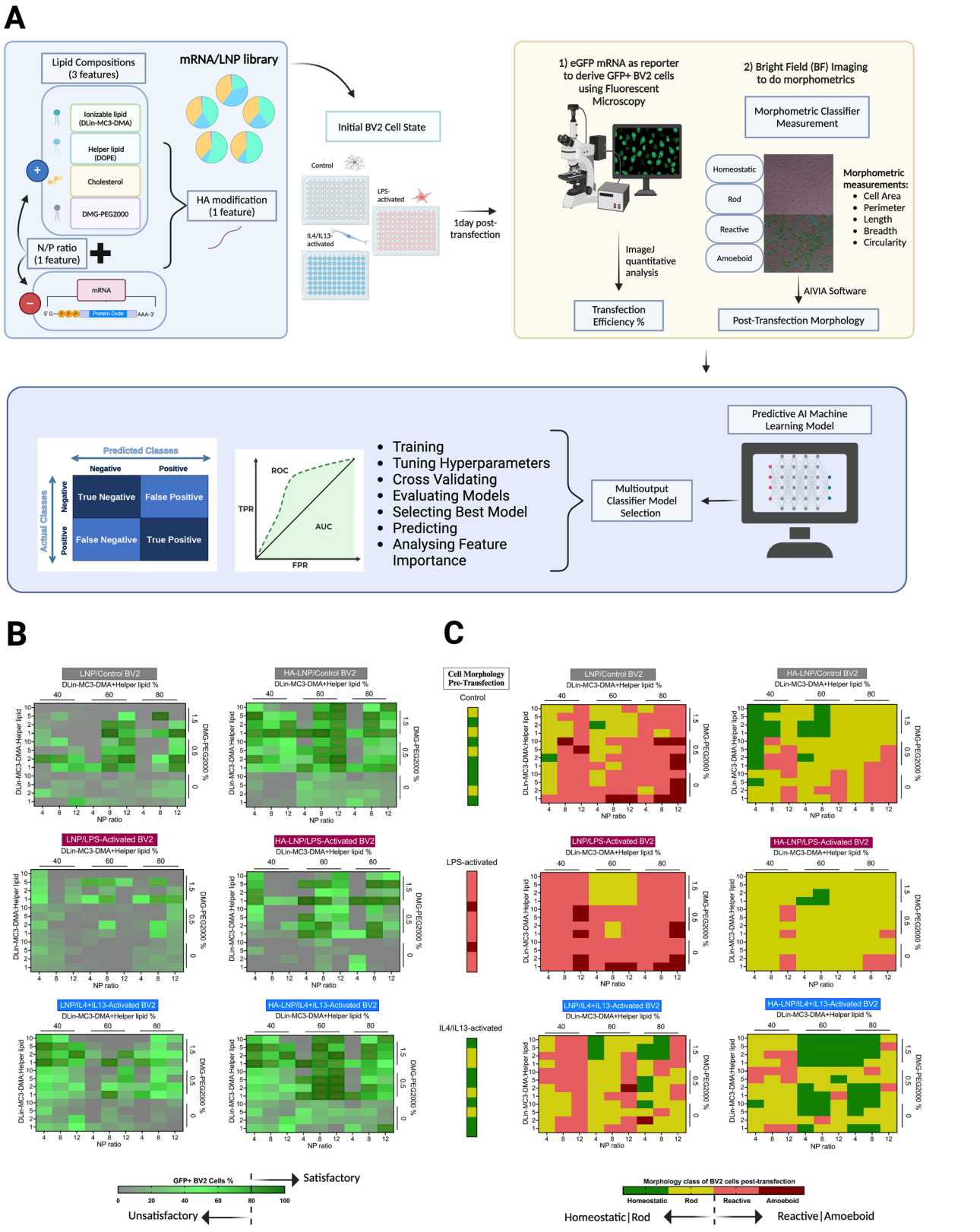

Figure 1. Overview of the screening methodology and results. (A) This schematic outlines the screening process, encompassing the preparation of the LNP library, transfection of various initial states of BV2 cells using the formulated LNPs, and subsequent analysis of outputs including transfection efficiency and post-transfection cell morphology. These data are then utilized to train a supervised multi-output classifier as an ML algorithm to identify the optimal model and assess its predictive performance. (B) A double gradient heat map illustrating the transfection efficiency of BV2 cells 24 h post-transfection, categorized by the percentage of GFP+ cells analyzed using ImageJ. Formulations achieving over 80% transfection efficiency are classified as satisfactory (indicated by dashed patterns), while those below this threshold are deemed unsatisfactory. (C) A categorical heat map depicting the morphology of BV2 cells post-transfection across different initial states. This map is based on morphometric data obtained from AIVIA software, where categories are assigned if more than 50% of cells in the frame belong to a specific morphology. For ML analysis, cells were classified into two groups: Homeostatic|Rod (when over 50% of cells fall into this category) and Reactive|Amoeboid (when over 50% fit this classification). Before transfection, BV2 cells exhibited a Homeostatic|Rod morphology in control and IL4/IL13-activated states, whereas they displayed a Reactive|Amoeboid morphology in LPS-activated states.

FESEM were employed to confirm the expected structural changes. The mean physicochemical characteristics of the LNP library presented an average diameter of 164.3 nm ± 8.6 for LNP formulations, while HA-LNP formulations have a mean size of 185.7 nm ± 9.2 as shown in Figure 2(A). Both formulations had PDI values less than 0.2, indicating low dispersity in size distribution. The surface charge, as indicated by the zeta potential, was 3.75 mV ± 1.6 for the LNP library and −12.0 mV ± 3.4 for the HA-LNP library. The encapsulation efficiency of mRNA in LNP library was measured at 71.4 ± 3.8, while the encapsulation efficiency for HA-LNP library was found to be 79.0 ± 6.0 (Figure 2(A)). The morphology studies conducted using FESEM and TEM on these formulations were consistent with the DLS results and are presented for two representative formulations, specifically MC3:DOPE:Chol:DMG-PEG2000 (40:20:38.5:1.5) with an N/P ratio of 8 (final mRNA concentration of 2 µg/ml) (Fig. S3). A reduction in the size of LNP but not HA-LNP was observed in TEM images. One reason could be the shrinkage of particles that occurs during the drying process for TEM sample preparation, which can lead to an apparent decrease in size. Additionally, the hydrodynamic layer surrounding the nanoparticles in solution may contribute to their effective size measurements in DLS being larger than what is observed in TEM. The presence of hyaluronic acid in HA-LNPs may provide structural stability, preventing significant size changes during imaging and preserving their original dimensions compared to standard LNPs. DOPE and DSPC are the two most common helper lipids used in the field for preparing LNPs. The exclusion of DPSC from the library was based on the results of initial transfection experiments. Results indicated that LNPs containing DOPE exhibited a five-fold increase in MFI compared to those with DSPC. Importantly, cell viability remained above 80% for both lipid formulations, showing no significant difference between the two groups in terms of cytotoxicity (Fig. S4). This notable difference in transfection efficiency can be attributed to the distinct structural properties and functionalities of DOPE and DSPC, which affect their behavior during endocytosis and subsequent endosomal escape (Medjmedj et al., 2022; Tang et al., 2023). Previous studies have demonstrated that LNPs formulated with DOPE yield higher transfection rates in Dendritic cells compared to those with DSPC. However, our study is the first to report the differential response of microglia cells to DOPE versus DSPC (Medjmedj et al., 2022). The cone-shaped structure of DOPE, characterized by unsaturated tails, facilitates the formation of non-lamellar phases, which promotes membrane fusion and destabilization- key factors for effective endosomal escape of mRNA (Medjmedj et al., 2022; Tang et al., 2023). In contrast, DSPC's cylindrical structure with saturated tails leads to stable bilayer formations. While this stability aids in the initial nanoparticle formation, it hinders the necessary membrane fusion for efficient mRNA release into the cytoplasm (Medjmedj et al., 2022; Tang et al., 2023). As a result, LNPs containing DSPC may become trapped within endosomes, leading to decreased transfection efficiency (Medjmedj et al., 2022; Tang et al., 2023). Given these insights and the superior transfection performance of DOPE observed in our experiments with microglia, we have opted to utilize DOPE exclusively as the helper lipid for constructing our library, thereby streamlining the screening process. By varying the lipid composition, N/P ratio, and HA modification, 216 formulations were prepared (Table 1). The range of lipid composition chosen was similar to a previous report (Zhu et al., 2024). Each LNP formulation was added to microglia BV2 cells pretreated as follows: 1) control (with no prior stimulation), 2) LPS-activated, and 3) IL4/IL13-activated. These experimental conditions were chosen to produce microglia with distinct immunological phenotypes that represent resting, pro-inflammatory and anti-inflammatory states.

Microglia cell (BV2) behavior in response to stimulation

The CLSM images reveal distinct morphological characteristics associated with different activation states (Figure 2(B)):

1. **LPS-activated state**: The majority of BV2 cells exhibited a rounded and flattened appearance with irregular cell bodies and thicker branches, reflecting the "Reactive" and "Amoeboid" morphology commonly associated with pro-inflammatory or M1-like microglial activation. The enlarged cell bodies suggest increased cellular activity and heightened production of inflammatory mediators (Bi et al., 2014; He et al., 2021; Xia et al., 2022). The reactive state represents a transient phase of pro-inflammatory activation, which can progress to an amoeboid phenotype if inflammation persists. In contrast, a smaller subset of cells displayed distinct morphological characteristics, including smaller and slightly elongated forms with thin branches, categorized as "Rod" and "Homeostatic" indicating a spectrum of activation responses within the population.
2. **IL4/IL13-activated state**: Most cells presented small somas and elongated processes, typical of the "Rod" morphology linked to M2-like or anti-inflammatory activation states, suggesting a shift toward neuroprotective and tissue-repair functions (Wang et al., 2019). However, some cells retained small somas and branches identified as "Homeostatic," and very few exhibited irregular shapes with larger somas, classified as "Reactive" and "Amoeboid," indicating that not all cells uniformly adopt the elongated phenotype in response to IL4/IL13 stimulation.
3. **Control (unstimulated)**: Under culture conditions devoid of specific activation stimuli, most cells displayed a "Homeostatic" state with small somas and very thin branches that are often not visible at low magnification, alongside slightly elongated cells resembling "Rod" morphology. Nonetheless, a minority of cells exhibited larger somas and irregular body shapes, referred to as "Reactive" and "Amoeboid" indicating inherent heterogeneity in the baseline state of these cells (Karunia et al., 2021).

These morphological observations align with previous studies on microglial activation states (Levi et al., 1998; Fernández-Arjona M del et al., 2019; Leyh et al., 2021;

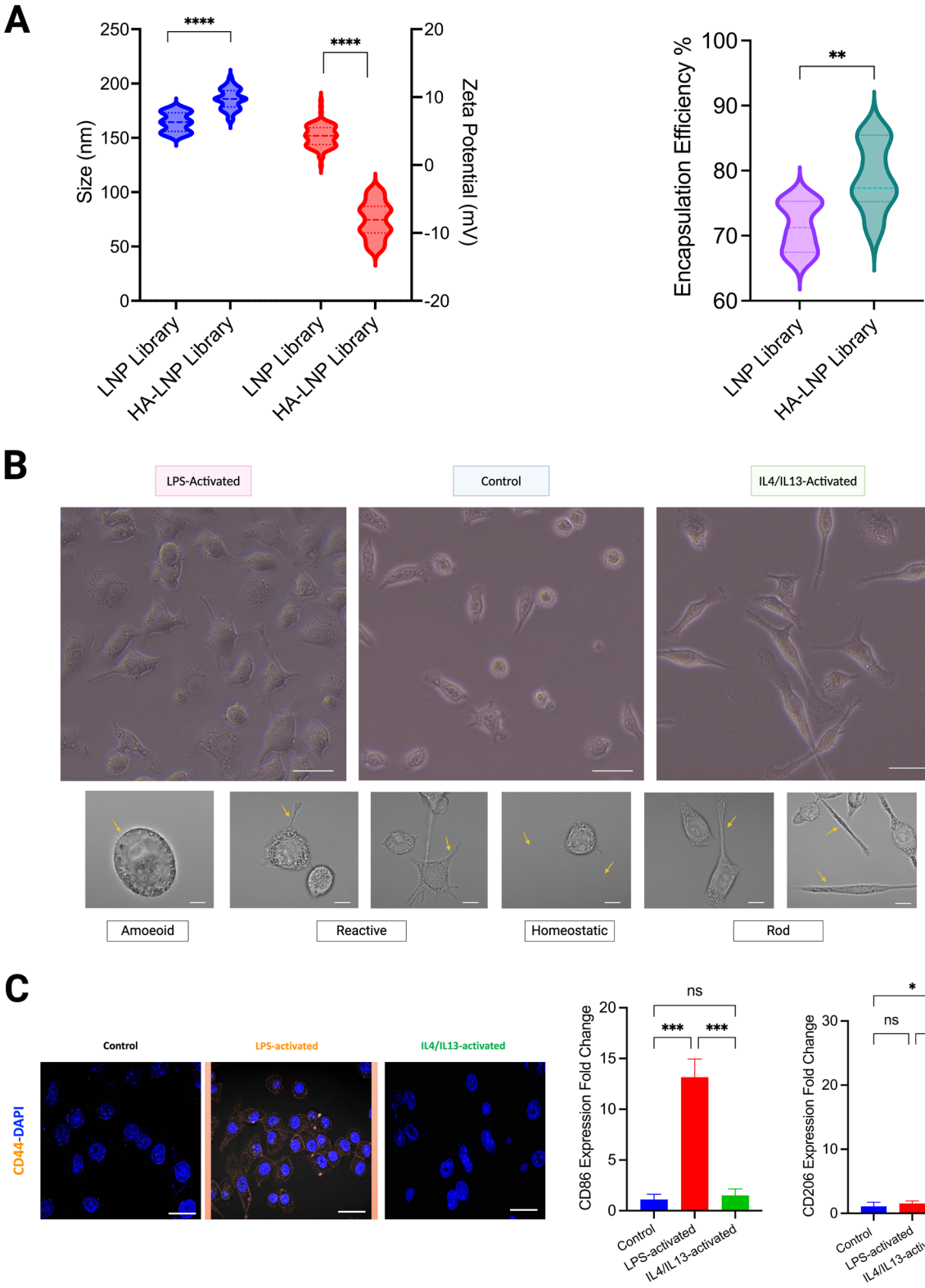

Figure 2. Cellular characterization and behavior. (A) Left: Bar chart displaying the average size (left blue bars) and zeta potential (right red bars) of LNP formulations (mean ± SD for all 108 libraries) and HA-LNP (mean ± SD for all 108 libraries). Right: Percentage of encapsulation efficiency for two different libraries of LNP and HA-LNP, based on a sample size of $n = 108$ for each library. (B) Confocal microscopy images of BV2 cells across various activation states at 40X (upper row) and 63X (bottom row) magnification. Scale bars: 50 µm (upper row) and 10 µm (bottom row). The major characteristics of each morphology are indicated by yellow arrows in the bottom row. From left to right: the amoeboid morphology features a very large soma with few short processes, appearing rounded; the reactive morphology displays irregular cell bodies with a large soma and thickened processes; the homeostatic morphology has a small soma with thin, highly branched processes; and the rod morphology exhibits an enlarged cell body with processes that create a polar shape. (C) Left: Immunostaining of BV2 cells in different activation states. Fixed cells were stained with anti-CD44 (orange) and DAPI (blue) for nuclear visualization. CD44 served as a marker for pro-inflammatory activated cells. The immunostaining images were captured using a confocal microscope (40X, scale bar: 50 µm). Right: qPCR results for BV2 cells with or without activation. The left bar plot compares the expression of the pro-inflammatory gene CD86 between control BV2 cells (blue bars), LPS-activated BV2 cells (red bar), and IL4/IL13-activated BV2 cells (green bar). The right bar plot compares the expression of the anti-inflammatory gene CD206 between control BV2 cells (blue bar), IL4/IL13-activated BV2 cells (green bar), and LPS-activated BV2 cells (red bar). β-actin was used as the reference gene for normalization. All experiments were conducted in triplicate, and the data are presented as the mean ± SD of the three independent replicates. P-values are indicated as follows: ****<0.0001, ***<0.0002, **<0.0021, *<0.0332, ns = not significant.

Choi et al., 2022). Additionally, q-PCR results confirmed that the observed morphological alterations were associated with significantly elevated expression levels of the pro-inflammatory marker CD86 in LPS-activated BV2 cells, which exhibited a fold change of 13.1 ± 1.8 compared to IL4/IL13-activated BV2 cells with a fold change of 1.5 ± 0.6 and control BV2 cells with a fold change of 1.1 ± 0.5. In contrast, the anti-inflammatory marker CD206 showed a fold change of 17.7 ± 7.1 in IL4/IL13-activated BV2 cells compared to LPS-activated BV2 cells, which had a fold change of 1.5 ± 0.4, and control BV2 cells with a fold change of 1.1 ± 0.6. These results support the morphological classification observed in Figure 2(C) (Right). The literature has shown that LPS-activated cells have bigger somas and irregular morphologies, which are related to higher production of pro-inflammatory cytokines (Choi et al., 2022). In contrast, the elongated morphology observed in IL4/IL13-activated cells is connected to the synthesis of anti-inflammatory mediators and proteins that promote tissue repair (Karunia et al., 2021). As a result, various morphological changes in microglial cells correspond to their immunological status and functional results. In this study, the morphological changes provide a visual indicator that can be used (in conjunction with other markers) to assess the efficacy of LNP and HA-LNP formulations in modulating microglial phenotypes. Variations in CD44 expression levels were observed when examining different activated BV2 cells. These cells were stimulated with either LPS or IL-4/IL-13 and evaluated through immunostaining with anti-CD44 antibody (orange). As depicted in Figure 2(C) (Left), CD44 expression was higher in LPS-stimulated BV2 compared to both the control group and cells activated by IL-4/IL-13. These findings align with prior research, in which studies indicated increased CD44 expression in pro-inflammatory-activated microglia (Matsumoto et al., 2012; Bradford et al., 2024). The enhanced CD44 expression on activated primary microglia from mice was also confirmed in transcriptomic analysis (oral communication with Prof. Nancy IP's research team, Life Science Department, The Hong Kong University of Science and Technology.)

High-throughput screening and machine learning analysis

The entire LNP library was tested across various microglial activation states. Transfecting LPS-activated BV2 was the most difficult, for which only 23 out of 216 formulations yielded satisfactory transfection efficiency (≥80%). In comparison, the success rate of transfection for unstimulated BV2 (39/216) and IL4/IL13-activated BV2 (43/216) was higher than that observed in LPS-activated cells (Figure 1(B)). HA modification appeared to improve the transfection independent of whether the microglia were initially unstimulated, LPS-activated or IL4/IL13 activated. Among the 7 formulations that attained 100% transfection, 6 of them were modified by HA. Regarding morphology before transfection, heterogeneity was observed across the 10 repeats in the 96-well plate culture, with Homeostatic|Rod as the major phenotype in unstimulated cells and IL4/IL13-activated cells, and Reactive|Amoeboid as the major phenotype in LPS-activated cells. After transfection, the microglial states were altered depending on the LNP formulations (Figure 1(C)). Certain formulations, such as those with HA modification and moderate N/P ratios, were more effective in maintaining an anti-inflammatory Homeostatic|Rod phenotype. In contrast, formulations without HA modification tended to induce a pro-inflammatory Reactive|Amoeboid phenotype even in control or IL4/IL13-activated cells, which could be beneficial for enhancing immunogenicity in glioblastoma treatment. These general observations provide a broad understanding of the dataset before delving into the machine learning analysis.

Our ML approach aimed to predict transfection efficiency and post-transfection morphology based on LNP formulation parameters across various microglial activation states. The outcomes were stratified into binary classifications for transfection efficiency and microglial morphology. Transfection efficiency was classified as satisfactory if it exceeded 80%, while efficiencies below this threshold were considered unsatisfactory. This classification was implemented to aid in the development of predictive models within an integrated dataset. Establishing this threshold aligns with established practices in the field and ensures that only experiments demonstrating high gene expression levels are included, thereby improving the reliability of our analyses (Ding et al., 2023). For morphology, two main categories were considered: Homeostatic|Rod (indicating an anti-inflammatory direction) and Reactive|Amoeboid (indicating a pro-inflammatory direction). Supervised classifier models (MLP, RF, SVM, and Naïve Bayes) were evaluated for each of the three distinct BV2 initial states (control, LPS-activation, and IL4/IL13-activation). Tables S4, S5, and S6 display the optimized hyperparameters used for training all models. The results indicate that the MLP model consistently outperformed the other models across various cellular states, achieving the highest weighted F1-scores that were significantly different (P-value < 0.05) from those of the other models (Fig. S5). Specifically, the MLP model attained scores of 0.82 for transfection efficiency and 0.80 for morphology in the Control state, and 0.84 and 0.91, respectively, in the LPS-activated state. In the IL4/IL13-activated state, it recorded scores of 0.84 for transfection efficiency and 0.79 for morphology. The performance of all models evaluated based on weighted F1-score across different initial cell states is summarized in the informative table presented in Figure 3(A).

In the control state, in addition to the MLP, the RF model achieved an F1-score of 0.78 for transfection efficiency and 0.79 for morphology; the SVM model achieved an F1-score of 0.77 for transfection efficiency and 0.75 for morphology, and the Naïve Bayes model achieved an F1-score of 0.80 for transfection efficiency and 0.76 for morphology. For the LPS-activated state, besides the MLP, the RF model reached an F1-score of 0.83 for transfection efficiency and 0.85 for morphology; the SVM model achieved an F1-score of 0.82 for transfection efficiency and 0.85 for morphology; and the Naïve Bayes model recorded an F1-score of 0.81 for transfection efficiency and 0.88 for morphology. In the IL4/IL13-activated state, in addition to the MLP, the RF model obtained an F1-score of 0.77 for transfection efficiency and 0.76 for morphology; the SVM model reached an F1-score of 0.78 for transfection efficiency and 0.68 for morphology; while the Naïve Bayes model recorded an F1-score of 0.76 for transfection efficiency and 0.81 for morphology. Weighted F1-scores analysis showed that the MLP model surpasses other

A

Multioutput Model	Weighted F1 Score					
	Control initial state		LPS-activated initial state		IL4/IL13-activated initial state	
	Transfection Efficiency	Cell Morphology	Transfection Efficiency	Cell Morphology	Transfection Efficiency	Cell Morphology
Random Forest Classifier	0.7821	0.7886	0.8329	0.8550	0.7717	0.7650
Neural Network (MLP)	0.8181	0.8050	0.8422	0.9066	0.8455	0.7857
Support Vector Machine (SVM)	0.7693	0.7520	0.8192	0.8489	0.7836	0.6856
Naïve Bayes Classifier	0.8000	0.7608	0.8143	0.8844	0.7629	0.8097

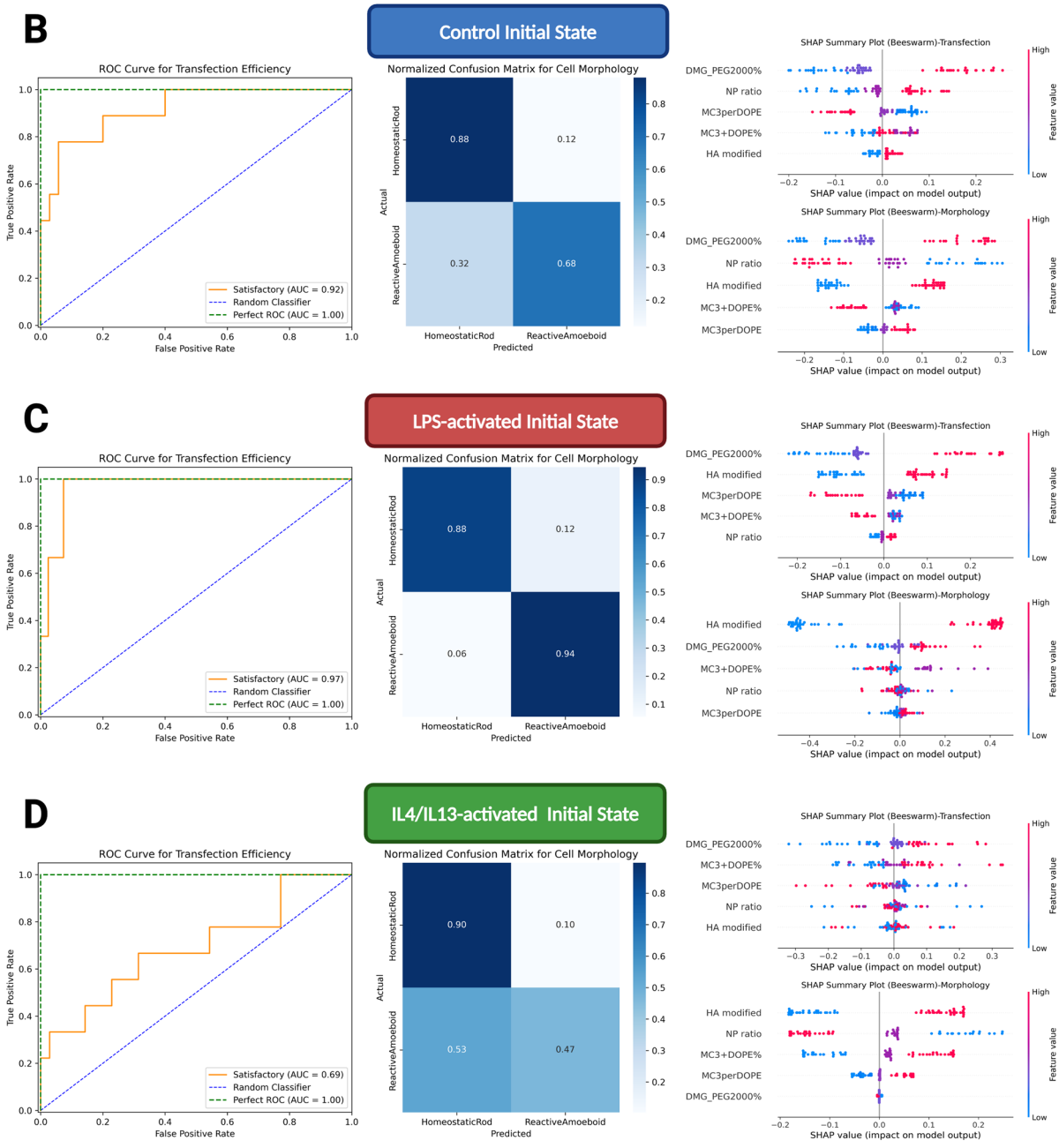

Figure 3. Machine learning analysis results for holdout test set across different models. (A) Comparison of the weighted F-score for the best models across various initial states of BV2 cells, focusing on outputs related to transfection efficiency (left group) and cell morphology (right group). The Neural Network (MLP) with optimized hyperparameters demonstrated the highest performance, presented as mean ± SD. Evaluation results table for the test dataset, detailing outputs from all considered supervised classifier models across different initial states of BV2 cells. (B) Prediction outcomes of the best model (MLP) for the control initial state. The left diagram displays the ROC curve for transfection efficiency output, with the satisfactory group identified as the positive class. The middle matrix represents the confusion matrix for cell morphology output, while the right diagram features the SHAP summary beeswarm plot, illustrating the impact of each feature on the model outputs for transfection (upper right) and cell morphology (lower right). (C) Prediction results of the best model (MLP) for the LPS-activated initial state, including the ROC curve for transfection efficiency output (left), confusion matrix for cell morphology output (middle), and SHAP summary beeswarm plot (right) showing feature impacts. (D) Prediction results of the best model (MLP) for the IL4/IL13-activated initial state, presented similarly with the ROC curve (left), confusion matrix (middle), and SHAP summary beeswarm plot (right) for transfection and cell morphology outputs.

models, including RF, SVM, and Naïve Bayes, in predicting transfection efficiency and morphology in different BV2 cellular states. While other models produced respectable values above 0.80 in some cases, the MLP performed particularly well in the LPS-activated state, with scores of 0.84 for transfection efficiency and 0.91 for morphology. These findings show the MLP model's effectiveness and potential for practical applications in diverse cellular environments. To investigate the interrelationships among the features, we conducted a Nested Pearson's correlation analysis. The results as shown in Fig. S6 are less than 0.001 for any binary correlation. This suggests minimal correlation among the features, implying that each feature contributes independently to the model predictions.

Consequently, the MLP model was the subject of the model prediction and SHAP analysis. The ROC curve for the binary task of transfection efficiency was plotted using the holdout test set, with satisfactory transfection defined as the true positive. The results, displayed in Figure 3(B, C and D) (Left columns), revealed that the area under the curve (AUC) was highest for the classifier of LPS-activated cells, scoring 0.97 (Figure 3(C)). This high AUC indicates an excellent ability of the model to distinguish between positive and negative transfections in LPS-activated cells, suggesting that it can accurately identify true positives while minimizing false positives. In contrast, the AUC for control state cells reached 92%, indicating strong predictive performance but slightly less than that of the LPS-activated state. For IL4/IL13-activated cells, however, the AUC was only 69%, reflecting a significant drop in predictive capability. This lower AUC suggests that the model struggles to differentiate between transfected and non-transfected states in this condition. The weaker predictive performance for IL4/IL13-activated microglia could be attributed to the biological complexity of the activation pathway, the limited representation of specific features in the hold-out test set, or inherent noise in the data. Overall, these AUC values illustrate the varying effectiveness of the MLP model across different cellular states and highlight areas where further data collection and refinement may be necessary to enhance predictive accuracy. Furthermore, confusion matrices for the multiclass cell morphology task were generated from the holdout test set and are presented in Figure 3(B, C and D) (Middle columns). These matrices indicate that the classifier is most accurate in predicting cell morphology post-transfection for microglia stimulated by LPS, achieving predictive capacities greater than 80% for both classes. In contrast, unstimulated microglia (control state) showed a prediction accuracy of over 80% for the Homeostatic|Rod class, but a lower predictive capacity (68%) for the Reactive|Amoeboid class. The MLP model demonstrated a low predictive capacity of 47% for Reactive|Amoeboid morphology in microglia activated by IL4/IL13, but a strong predictive capacity of 90% for the Homeostatic|Rod class. Due to the Reactive|Amoeboid class's lower distribution in both the control and IL4/IL13-activated states—less than 30% in the former and less than 45% in the latter—compared to over 45% in the LPS-activated state, this limitation is most likely caused by this. This indicates that further data may be required for model improvement. Nonetheless, the MLP model still predicts Homeostatic|Rod morphology effectively following transfection in both control and IL4/IL13-activated states.

To gain deeper insights into the factors governing LNP-mediated transfection efficiency and microglial phenotype modulation, we employed SHAP analysis using the holdout test set. The desired output for transfection efficiency was set to the "satisfactory" class, while the desired output for morphology was biased toward "Homeostatic|Rod" for all cell states. This approach effectively identified the most influential formulation parameters for each initial microglial activation state, as illustrated in Figure 3(B, C and D) (Right columns), with the mean SHAP values for each state provided in Fig. S7. For control BV2 cells, the top features impacting transfection efficiency were high DMG-PEG2000%, high N/P ratio, and low to moderate MC3perDOPE. In contrast, the primary features affecting morphology were high DMG-PEG2000%, low N/P ratio, and HA modification. This suggests that while HA plays a crucial role in maintaining desired morphology (Homeostatic|Rod) post-transfection, lipid composition, and N/P ratio are more significant for transfection efficiency in unstimulated microglia. A high N/P ratio enhances transfection efficiency by improving the electrostatic interactions between cationic transfection agents and negatively charged mRNA, facilitating cellular uptake. However, this high ratio can also lead to a shift toward a reactive or amoeboid morphology in cells due to increased stress responses triggered by the higher charge density.

The SHAP analysis of LPS-activated BV2 cells revealed that high DMG-PEG2000%, HA modification, and low to moderate MC3perDOPE were the most impactful features for transfection efficiency. For morphology, the key features were HA modification moderate to high DMG-PEG2000%, and moderate MC3 + DOPE%. These findings highlight the specific formulation requirements necessary for effectively transfecting and modulating the behavior of LPS-activated microglia, which are typically challenging to target. Notably, HA modification emerged as the most influential feature, underscoring its essential role in enhancing transfection efficiency and promoting anti-inflammatory morphological changes. The improved transfection efficiency observed with the incorporation of HA into the LNP structure is consistent with experimental data. This finding also aligns with previous studies indicating that HA's ability to engage CD44 can downregulate microglial inflammation by suppressing TLR4, the primary pathway activated by LPS (Liu et al., 2014).

According to the SHAP analysis for IL4/IL13-activated cells, the main features affecting transfection output were identified as DMG-PEG2000%, MC3 + DOPE%, and MC3perDOPE. For morphology, the key parameters included HA modification, N/P ratio, and MC3 + DOPE%, with mean SHAP values provided in Fig. S7. This highlights the significance of HA modification, especially in anti-inflammatory--activated cells. If the aim is to enhance immunogenicity for treating tumor-resistant microglial cells in glioblastoma, formulations that do not incorporate HA modification could be explored. However, given the limitations noted in the performance of the ML model, we revisited and analyzed our experimental data shown in Figure 1(B and C) to gain deeper insights into cell behavior. Our analysis involved

systematically comparing the mean contributions of features derived from our experimental data with the mean absolute SHAP values obtained from our machine learning model. To facilitate this comparison, we created Table S7, which presents a comprehensive overview of feature importance based on both experimental data and SHAP analysis. This table includes the ranked mean contributions of features to transfection efficiency and morphology, normalized to a scale of 0 to 1, alongside their corresponding mean absolute SHAP values. Interestingly, while the SHAP analysis identified DMG-PEG2000%, MC3 + DOPE%, and MC3perDOPE as significant features with the highest mean SHAP values for transfection output (as shown in Fig. S7), our empirical analysis indicated that DMG-PEG2000%, MC3perDOPE, and HA modification were the top three ranked features based on experimental observations (Table S7). We quantified the average contributions of these top five features and compared them with their respective SHAP values to provide a clearer understanding of their relative importance. For morphological assessments, we observed that the ranking from the SHAP analysis aligned more closely with our experimental findings, highlighting HA modification, N/P ratio, and MC3 + DOPE% as the three most influential features. This comparison underscores the complexities inherent in interpreting machine learning results within biological contexts and emphasizes the critical need for validating computational models with empirical data. The ML analysis guides to design of LNP carriers not only to attain effective transfection but also to maintain or direct microglia toward anti-inflammatory phenotypes. These formulations will be most suitable for delivering mRNA cargo to suppress over-reactive microglia, such as those associated with neurodegenerative disease and ocular inflammation. The ML analysis can also be informative for applications that benefit from immunogenic microglia, such as the treatment to overcome the immunosuppressive tumor environment of glioblastoma. In this case, the pro-inflammatory Reactive|Amoeboid is the preferred morphology post-transfection. Thus, the aforementioned approach is useful for the strategic design of LNP formulations for customized therapeutic interventions to specific cellular contexts and intended outcomes.

Validation of ML prediction on LPS-activated microglia

We further validated the MLP model, which was found to work best for LPS-activated BV2 microglia, by checking its performance on four unseen samples. In the meantime, we intended to identify a suitable LNP formulation to deliver mRNA that encodes IL10, an anti-inflammatory cytokine whose deficiency can trigger a pro-inflammatory switch in microglia (Saraiva & O'Garra, 2010; Guillot-Sestier et al., 2015; Laffer et al., 2019; Wang et al., 2021). Recent research by Gao et al. (2024) on ischemic brain conditions has shown that the delivery of IL10 mRNA can repolarize microglia to an anti-inflammatory phenotype. We reason that an LNP carrier capable of transfecting and immunomodulating microglia can be broadly applicable for delivering mRNA cargo against neuroinflammation. The four unseen LNP formulations as well as the predicted performance according to the previously trained MLP model, were listed in Table 2. They were annotated as LNP1, LNP2, HA-LNP1 and HA-LNP2. The last two differed from the first two only by the HA modification. The findings from ML analysis confirmed the importance of HA modification in improving transfection efficiency and driving a shift in microglial polarization toward an anti-inflammatory phenotype, especially in activated cells. This motivated us to include HA as a key distinguishing feature.

The model predicted that among these formulations, HA-LNP2 would meet our objectives for attaining satisfactory transfection efficiency and yielding Homeostatic|Rod morphology. In contrast, the other formulations were expected to yield unsatisfactory transfection efficiencies, with LNP1 predicted to perform the worst by inducing a Reactive|Amoeboid morphology, which is undesirable for inflammatory-related treatment. First, we examined the in vitro results and analyzed the experimental outcomes for these four formulations using eGFP mRNA. The ML model accurately predicted that only HA-LNP2 would achieve satisfactory transfection efficiency (over 80% GFP-positive cells), while the other formulations demonstrated lower efficiencies, as shown in Table 2. Figure 4(A) is representing the bright field and fluorescent images of four formulations, juxtaposed Lipofectamine MMAX, to show the experimental validation results. To further explore the interaction of HA-LNP2 with LPS-activated BV2 cells, we performed cellular uptake studies using a CD44 blocking assay. The results confirmed that the enhanced uptake of HA-LNP2 was primarily mediated by CD44 receptors, which are upregulated in LPS-activated microglia, as shown in Figure 4(C). Morphological assessments revealed that cells treated with HA-LNP1 and HA-LNP2 adopted Homeostatic|Rod morphology, while those treated with LNP1 and LNP2 showed an increase in soma size and shift toward Reactive|Amoeboid morphology, refer to Figure 4(A) (BF images). BF images for all four formulations are presented in

Table 2. Machine learning predictions for validation formulations.

	Input1	Input2	Input3	Input4	Input5	Output1	Output2
	MC3+ DOPE%	DMG_ PEG2000%	MC3per DOPE	N/P ratio	HA modified	Transfection	Cell Morphology
LNP1	60	1.5	4.3	20	No	Unsatisfactory	Reactive|Amoeboid
HA-LNP1	60	1.5	4.3	20	Yes	Unsatisfactory	Homeostatic|Rod
LNP2	60	1.5	1.72	5	No	Unsatisfactory	Homeostatic|Rod
HA-LNP2	60	1.5	1.72	5	Yes	Satisfactory	Homeostatic|Rod

This table indicates the predicted outputs for transfection efficiency and cell morphology of validation formulations, prepared in vitro, using the best-performing model (MLP) for the LPS-activated initial state of BV2 cells. The input columns include the percentage of MC3 and DOPE, the percentage of DMG-PEG2000, the ratio of MC3 to DOPE, the N/P ratio, and the presence or absence of HA modification. The predicted outputs for transfection efficiency and cell morphology are provided in the last two columns.

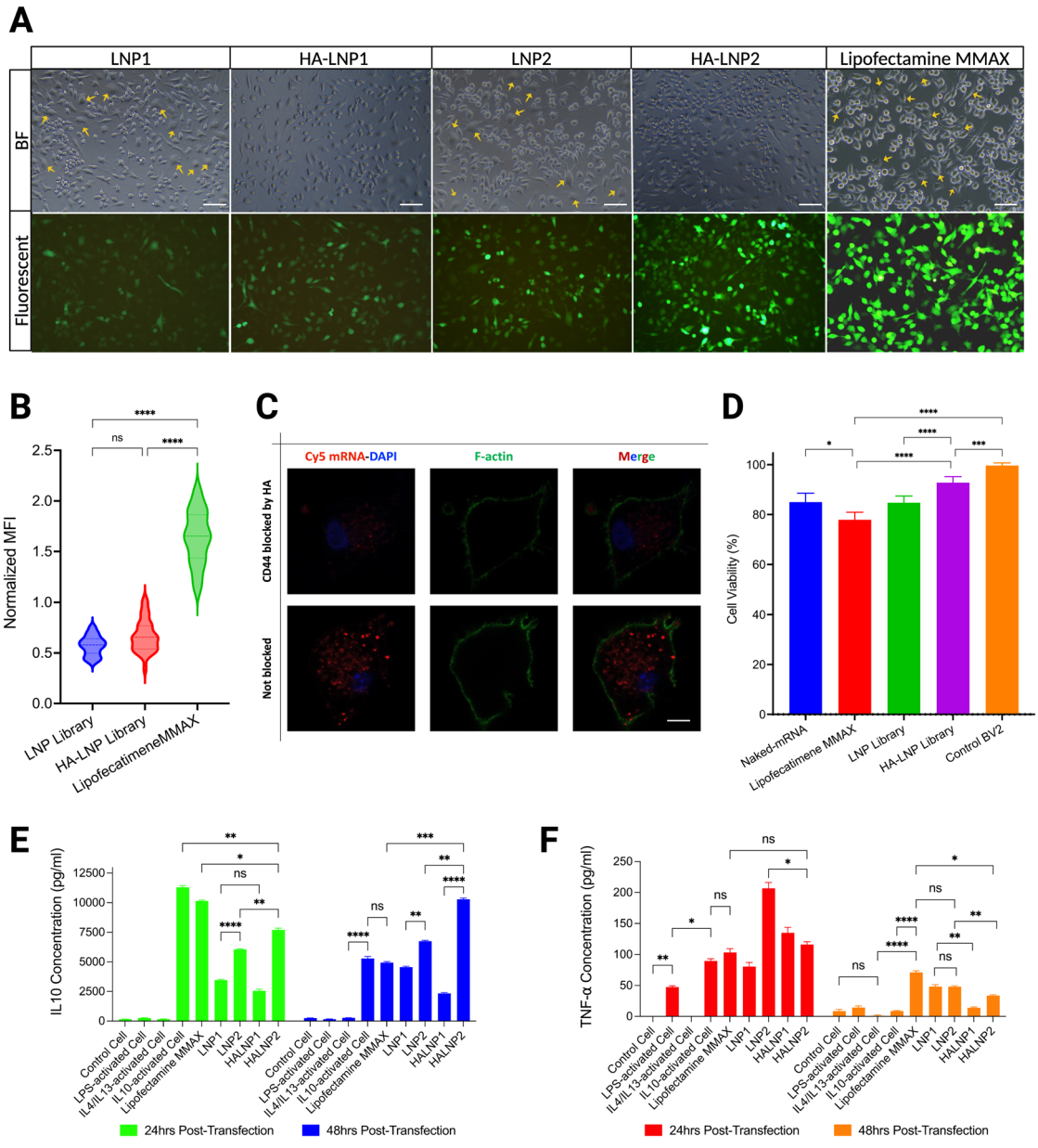

Figure 4. Validation of ML prediction on LPS-activated BV2 cells. (A) Fluorescence microscopy images of LPS-activated BV2 cells transfected with eGFP mRNA 24 h post-transfection. The top row shows bright-field images, while the bottom row displays fluorescent images captured using a fluorescence microscope (20X magnification, scale bar: 50 µm). LNP2 and HA-LNP2 are the same formulations used to validate the machine learning prediction. Lipofectamine MMAX was used as a control with the same mRNA dosage (final mRNA concentration of 2 µg/ml). (B) Normalized mean fluorescence intensity (MFI) after transfection with eGFP mRNA, quantified using ImageJ analysis, with lipofectamine MMax as a positive control. The sample sizes for both LNP and HA-LNP libraries are $n = 108$. (C) Blocking (competition) assay to evaluate the CD44 targeting capability of HA-LNP formulations. The MC3:DOPE:Chol:DMG-PEG2000 (40:20:38.5:1.5) formulation with an N/P ratio of 8 (final mRNA concentration of 2 µg/ml) was used to transfect LPS-activated BV2 cells under two conditions: Top row) BV2 cells treated with HA solution, bottom row) BV2 cells without blocking. Four hours post-transfection with Cy5-mRNA (red), cells were fixed, and the nucleus (DAPI) and F-actin (phalloidin, green) were stained to visualize the internalized mRNA (red). The immunostaining images were captured using a confocal microscope (63X magnification, scale bar: 10 µm). (D) Average bar plot illustrating the percentage of BV2 cell viability as determined by the MTT assay for various LNP groups (mean ± SD) and HA-LNP (mean ± SD), including controls: blank BV2 cells, naked mRNA, and commercial LipofectamineMMAX carrier encapsulated mRNA (mean ± SD). The mRNA cargo utilized was eGFP mRNA. (E) IL-10 ELISA assay results show cytokine secretion from LPS-activated BV2 cells at two time points post-transfection: 24 h (green bars) and 48 hours (blue bars). Data are presented for different formulations as carriers for IL-10 mRNA ($n = 3$). (F) TNF-α ELISA assay results for TNF-α cytokine secretion from LPS-activated BV2 cells at the same time points: 24 h (red bars) and 48 h (orange bars) across different formulations ($n = 3$). P-values are indicated as follows: **** <0.0001, *** <0.0002, ** <0.0021, * <0.0332, ns = not significant.

Figure 4(A) and the yellow arrows are indicating the shift toward Reactive|Amoeboid morphology for LNP1, and LNP2 formulations.

The model predicted cells to adopt Homeostatic|Rod after transfection by LNP2. This however contrasted with the experimental observation. The discrepancy shows the shortfall of the ML model and there is room to improve the accuracy by expanding the training data. We compared the experimental results with those obtained using the commercial transfection reagent, Lipofectamine MMAX (Figure 4(A and B)). Note that while Lipofectamine MMAX demonstrated high transfection efficiency with even higher MFI than our formulations, it was more immunogenic and tended to promote the Reactive|Amoeboid morphology. Compared to

HA-LNP, Lipofectamine MMAX was more toxic to cells, as shown by the lower cell viability from the MTT assay (Figure 4(D)). While the protein expression per microglia is an important measure, it should not be the only criterion for assessing carrier suitability. It is crucial to consider both the biocompatibility and the immunological effect of the transfection agents. HA-LNP2 is therefore considered a superior mRNA carrier if the goal is to mitigate inflammation.

Next, we encapsulated IL10 mRNA into the four formulations, with the expectation that HA-LNP2 would yield the best transfection efficiency based on preliminary data. The ELISA results demonstrated that the LNP2 formulation transfected cells with higher efficiency, yielding an IL10 expression of 6050 pg/ml ± 52, nearly double that of LNP1, which had an expression of 3461 pg/ml ± 72 after one day. This observation aligns with our machine learning SHAP analysis (Figure 3(C) Right), indicating that the MC3perDOPE feature had an inverse effect on transfection efficiency, suggesting that reducing this feature would enhance overall performance. Furthermore, the HA-LNP2 formulation exhibited markedly higher IL10 protein expression, reaching up to 10,287 pg/ml ± 112 for sustained expression after two days, compared to LNP2's IL10 expression of 6755 pg/ml ± 63, as shown in Figure 4(E). This finding is consistent with our ML SHAP analysis (Figure 3(C) Right), which identified HA modification as one of the top three influential features positively impacting transfection efficiency. The level of protein expression achieved with HA-LNP2 is comparable to that observed in cells treated directly with 100 ng/ml of IL10 cytokine, which resulted in an IL10 detection of 5295 pg/ml ± 165 after two days. In contrast, HA-LNP1 did not enhance IL10 expression, recording a level of 2557 pg/ml ± 134 compared to LNP1's level of 3461 pg/ml ± 72 after one day, and HA-LNP1 showed a further decrease in IL10 expression after two days, reaching 2339 pg/ml ± 70. As a positive control for transfection, Lipofectamine MMAX demonstrated high levels of IL10 expression at 10,146 pg/ml ± 70 on day one but experienced a two-fold reduction by day two, resulting in an IL10 expression of 4942 pg/ml ± 80 at the end of the observation period. Therefore, after 2 days of transfection, HA-LNP2 exhibited the highest transfection efficiency with the target gene and induced a polarization of cell morphology toward the Homeostatic|Rod shape, which is also consistent with the ML predictions.

The secretion of TNF-α remains another hallmark indicative of inflammatory microglia. ELISA results revealed that after one day, the LNP2 formulation elevated TNF-α expression to 207 pg/ml ± 9; however, this level dropped to below 100 pg/ml across all formulations by the second day (Figure 4(F)). Among the formulations tested after 2 days, the commercial Lipofectamine MMAX exhibited the highest TNF-α expression at 71 pg/ml ± 3, which was greater than that of the HA-LNP2 formulation, recorded at 33 pg/ml ± 1. Notably, after 2 days of transfection, HA-LNP2 demonstrated approximately a four-fold reduction in TNF-α levels compared to its expression on the first day, while LNP2 also showed a similar four-fold decrease, resulting in a TNF-α level of 48 pg/ml ± 2. This reduction in TNF-α expression may be attributed to the synergistic effects of IL10 mRNA functioning as an anti-inflammatory agent in conjunction with these carriers. Previous studies have indicated that IL10 cytokine inhibits early-stage TNF-α production in LPS-stimulated macrophage cell lines (RAW264.7) by decreasing MyD88 production and impairing NF-κB activation (Dagvadorj et al., 2008). These findings suggest that the HA-LNP formulation not only boosts IL10 expression but also effectively suppresses pro-inflammatory responses. Our results revealed that although the IL10-activated cells as positive control exhibited a high level of expression at 24 h, this expression significantly decreased thereafter. This finding is consistent with previous studies that have noted the transient nature of IL10's effects, underscoring the necessity for sustained delivery of anti-inflammatory signals through mRNA-based therapies (Nadeau and Rivest, 1999; Dagvadorj et al., 2008).

Finally, to assess the inflammatory induction of the carriers without the interference of anti-inflammatory IL10 mRNA, we performed the RAW-Blue assay. This genetically modified RAW264.7 cell line exhibits a color change upon activation of NF-κB, a transcription factor that plays a central role in the innate immune response, particularly in regulating pro-inflammatory cytokines and chemokines. The NF-κB pathway serves as a vital link between the innate and adaptive immune systems, orchestrating the production of inflammatory mediators in response to different stimuli. Our findings indicate that the HA-LNP2 formulation, when loaded with reporter eGFP mRNA, resulted in an NF-κB activity of 0.046 ± 0.003. Statistical analysis revealed that this value did not show a significant difference when compared to the untreated controls, which exhibited an NF-κB activity of 0.062 ± 0.001 (Fig. S8). In contrast, the positive control group subjected to LPS activation displayed a markedly higher NF-κB activity of 0.646 ± 0.018. Furthermore, HA-LNP2 maintained a low NF-κB activity of 0.05 ± 0.002 while effectively delivering IL10 mRNA, in comparison to the significantly elevated levels observed in cells activated with recombinant IL10, which showed NF-κB activity of 0.123 ± 0.002 (Fig. S8). These results underscore the potential therapeutic applications of HA-LNP2 in conditions characterized by excessive inflammation, as it effectively sustains low NF-κB activity while delivering anti-inflammatory mRNA.

To determine the best-performing LNP formulation on BV2 cell line, we trained a machine learning model in previous sections of this research. In this part, we seek to ascertain whether applying the best-performing formulation, HA-LNP2, to human iPSC-derived microglia (iMG) produces comparable outcomes. In order to connect microglial cell lines and human microglia and increase the translational potential of our findings for therapeutic applications, this comparison was essential. iMG are widely acknowledged as a robust model for primary human microglia due to their well-characterized properties and ability to accurately reflect human microglial functions (Abud et al., 2017). This choice allows for a more precise assessment of microglial responses to inflammatory stimuli and therapeutic interventions compared to conventional transformed cell lines. Importantly, iMG retain key functional characteristics and phenotypic traits essential for investigating neuroinflammatory processes linked to various diseases, including neurodegenerative, infectious, and autoimmune disorders (Abud et al., 2017; Jiang & Jin, 2023; Chadarevian et al., 2024; Douvaras et al., 2024). Here, we transfected LPS-activated iMG

with eGFP mRNA using HA-LNP2, the formulation predicted by our ML model and previously validated on the BV2 cell line. As shown in Fig. S9, we evaluated transfection efficiency, cell morphology, and cell viability one day post-transfection. The HA-LNP2 formulation resulted in a Homeostatic|Rod morphology, whereas the commercial transfection reagent Lipofectamine MMAX induced a Reactive|Amoeboid morphology, as highlighted by yellow arrows indicating reactive and moeboid cells. The machine learning model accurately predicted that HA-LNP2 would achieve over 80% transfection efficiency, a result confirmed in iMG. While the transfection efficiency of HA-LNP2 was statistically comparable to that of Lipofectamine MMAX, the MFI for HA-LNP2 (2±0.1) was lower than that of Lipofectamine MMAX (2.6±0.2). Additionally, cell viability analysis revealed that cells treated with Lipofectamine MMAX exhibited reduced viability (70.2±8%), whereas HA-LNP2 demonstrated minimal cellular toxicity with a viability rate of 100.1±6% compared to control cells. These results indicate that HA-LNP2 is an effective transfection agent for human iMG, capable of delivering mRNA to inflammatory-associated microglial cells while modulating their immune response. Overall, this study not only supports our previous findings but also establishes an important link between our results and potential therapeutic applications in human health contexts. By employing iMG as a model system, we enhance the translational relevance of our research and lay the groundwork for future investigations aimed at developing innovative treatments for neuroinflammatory diseases.

Conclusions

This study has employed a comprehensive library of LNP formulations, advanced ML techniques, and validation experiments to investigate mRNA delivery by LNPs and the carriers' influence on the microglial activation states. This approach could guide the formulation of LNP to attain both transfection efficiency and favorable immunological changes. Our findings highlight the application of HA-modified LNPs in transfecting pro-inflammatory activated microglia while skewing the cells toward anti-inflammatory phenotypes. The SHAP analysis further revealed that the dependence of microglial response on lipid composition, HA modification, and N/P ratio varied among different activation states. The ML-predicted HA-LNP formulation for IL10 mRNA delivery demonstrated a promising application, marked by enhanced IL10 expression and reduced levels of pro-inflammatory markers. Furthermore, the effectiveness of HA-LNP2 in regulating inflammatory responses has been proven by testing it on human iPSC-derived microglia (iMG). Overall, this study not only deepens our understanding of LNP-mediated mRNA delivery to microglia but also establishes a solid framework for the rational design and optimization of mRNA therapeutics, paving the way for the accelerated development of innovative treatments for neuroinflammatory disorders.

Acknowledgments

The authors would like to express their gratitude to the Biosciences Central Research Facility at HKUST (Clear Water Bay) for their provision of research facilities. All figures were created with BioRender.com.

Author contributions

Y. Chau, M. Rafiei, and A. Shojaei were responsible for initiating and conceptualizing the research project. M. Rafiei performed all the experiments and developed the Machine Learning models. Additionally, M. Rafiei authored the original draft of the manuscript. The writing, review, and editing processes were collaboratively contributed by Y. Chau, M. Rafiei, and A. Shojaei. Throughout the project, Y. Chau and A. Shojaei provided supervision and guidance.

Disclosure statement

Ying Chau is an associate editor of this journal. She had no part in the peer review or decision-making on this paper. The remaining authors declare no conflict of interest.

Funding

Research for this work was supported by the Hong Kong Research Grants Council (GRF 16102721), and the Hong Kong Innovation and Technology Commission (ITC CNERC14SC01).

Data availability statement

The data supporting this article have been included as part of the Supplementary Information.

References

Abud EM, Ramirez RN, Martinez ES, et al. (2017). iPSC-derived human microglia-like cells to study neurological diseases. Neuron 94:278–93. e9. doi: 10.1016/j.neuron.2017.03.042.

Au NPB, Ma CHE. (2017). Recent advances in the study of bipolar/rod-shaped microglia and their roles in neurodegeneration. Front Aging Neurosci 9:128. Available at https://www.frontiersin.org/journals/aging-neuroscience/articles/10.3389/fnagi.2017.00128/full [last accessed 27 Aug 2024] doi: 10.3389/fnagi.2017.00128.

Barbier AJ, Jiang AY, Zhang P, et al. (2022). The clinical progress of mRNA vaccines and immunotherapies. Nat Biotechnol 40:840–54. doi: 10.1038/s41587-022-01294-2.

Bi W, Zhu L, Jing X, et al. (2014). Rifampicin improves neuronal apoptosis in LPS-stimulated co-cultured BV2 cells through inhibition of the TLR-4 pathway. Mol Med Rep 10:1793–9. doi: 10.3892/mmr.2014.2480.

Bradford BM, Walmsley-Rowe L, Reynolds J, et al. (2024). Cell adhesion molecule CD44 is dispensable for reactive astrocyte activation during prion disease. Sci Rep 14:13749. doi: 10.1038/s41598-024-63464-3.

Buckley C, Murphy EJ, Montgomery TR, Major I. (2022). Hyaluronic acid: a review of the drug delivery capabilities of this naturally occurring polysaccharide. Polymers (Basel) 14:3442. doi: 10.3390/polym14173442.

Chadarevian JP, Hasselmann J, Lahian A, et al. (2024). Therapeutic potential of human microglia transplantation in a chimeric model of CSF1R-related leukoencephalopathy. Neuron 112:2686–707.e8. doi: 10.1016/j.neuron.2024.05.023.

Chen D, Love KT, Chen Y, et al. (2012). Rapid discovery of potent siRNA-containing lipid nanoparticles enabled by controlled microfluidic formulation. J Am Chem Soc 134:6948–51. doi: 10.1021/ja301621z.

Cherry JD, Olschowka JA, O'Banion MK. (2014). Neuroinflammation and M2 microglia: the good, the bad, and the inflamed. J Neuroinflammation 11:98. doi: 10.1186/1742-2094-11-98.

Choi S, Guo L, Cordeiro MF. (2021). Retinal and brain microglia in multiple sclerosis and neurodegeneration. Cells 10:1507. doi: 10.3390/cells10061507.

Choi S, Hill D, Guo L, et al. (2022). Automated characterisation of microglia in ageing mice using image processing and supervised machine learning algorithms. Sci Rep 12:1806. doi: 10.1038/s41598-022-05815-6.

Dagvadorj J, Naiki Y, Tumurkhuu G, et al. (2008). Interleukin-10 inhibits tumor necrosis factor-α production in lipopolysaccharide-stimulated RAW 264.7 cells through reduced MyD88 expression. Innate Immun 14:109–15. doi: 10.1177/1753425908089618.

Ding DY, Zhang Y, Jia Y, Sun J. (2023). Machine learning-guided lipid nanoparticle design for mRNA delivery. arXiv. Available from: http://arxiv.org/abs/2308.01402 [last accessed 19 Aug 2024].

Douvaras P, Buenaventura DF, Sun B, et al. (2024). Ready-to-use iPSC-derived microglia progenitors for the treatment of CNS disease in mouse models of neuropathic mucopolysaccharidoses. Nat Commun 15:8132. doi: 10.1038/s41467-024-52400-8.

Fan W, Huang W, Chen J, et al. (2022). Retinal microglia: Functions and diseases. Immunology 166:268–86. doi: 10.1111/imm.13479.

Fernández-Arjona M del M, Grondona JM, Fernández-Llebrez P, López-Ávalos MD. (2019). Microglial morphometric parameters correlate with the expression level of IL-1β and allow identifying different activated morphotypes. Front Cell Neurosci 13:472. doi: 10.3389/fncel.2019.00472.

Gao C, Jiang J, Tan Y, Chen S. (2023). Microglia in neurodegenerative diseases: mechanism and potential therapeutic targets. Signal Transduct Target Ther 8:359. doi: 10.1038/s41392-023-01588-0.

Gao M, Li Y, Ho W, et al. (2024). Targeted mRNA nanoparticles ameliorate blood-brain barrier disruption postischemic stroke by modulating microglia polarization. ACS Nano 18:3260–75. doi: 10.1021/acsnano.3c09817.

Ginhoux F, Lim S, Hoeffel G, et al. (2013). Origin and differentiation of microglia. Front Cell Neurosci 7:45. doi: 10.3389/fncel.2013.00045.

Giordano KR, Denman CR, Dubisch PS, et al. (2021). An update on the rod microglia variant in experimental and clinical brain injury and disease. Brain Commun 3:fcaa227.

Guillot-Sestier M-V, Doty KR, Gate D, et al. (2015). Il10 deficiency rebalances innate immunity to mitigate Alzheimer-like pathology. Neuron 85:534–48. doi: 10.1016/j.neuron.2014.12.068.

Guo X, Wang H, Li Y, et al. (2019). Transfection reagent Lipofectamine triggers type I interferon signaling activation in macrophages. Immunol Cell Biol 97:92–6. doi: 10.1111/imcb.12194.

Guo S, Wang H, Yin Y. (2022). Microglia polarization from M1 to M2 in neurodegenerative diseases. Front Aging Neurosci 14:815347. [Internet]. Available at: doi: 10.3389/fnagi.2022.815347.

Han X, Zhang H, Butowska K, et al. (2021). An ionizable lipid toolbox for RNA delivery. Nat Commun 12:7233. doi: 10.1038/s41467-021-27493-0.

Hayward SL, Wilson CL, Kidambi S. (2016). Hyaluronic acid-conjugated liposome nanoparticles for targeted delivery to CD44 overexpressing glioblastoma cells. Oncotarget 7:34158–71. doi: 10.18632/oncotarget.8926.

He Y, Taylor N, Yao X, Bhattacharya A. (2021). Mouse primary microglia respond differently to LPS and poly(I:C) in vitro. Sci Rep 11:10447. doi: 10.1038/s41598-021-89777-1.

Hou X, Zaks T, Langer R, Dong Y. (2021). Lipid nanoparticles for mRNA delivery. Nat Rev Mater 6:1078–94. doi: 10.1038/s41578-021-00358-0.

Hu D, Mezghrani O, Zhang L, et al. (2016). GE11 peptide-modified and reduction-responsive hyaluronic acid-based nanoparticles induced higher efficacy of doxorubicin for breast carcinoma therapy. Int J Nanomedicine 11:5125–47. doi: 10.2147/IJN.S113469.

Jarzebska NT, Frei J, Lauchli S, et al. (2021). Lipofection with synthetic mRNA as a simple method for T-cell immunomonitoring. Viruses 13:1232. doi: 10.3390/v13071232.

Jiang P, Jin M. (2023). Replacing microglia to treat Alzheimer's disease. Cell Stem Cell 30:1001–3. doi: 10.1016/j.stem.2023.07.005.

Karlstetter M, Scholz R, Rutar M, et al. (2015). Retinal microglia: just bystander or target for therapy? Prog Retin Eye Res 45:30–57. doi: 10.1016/j.preteyeres.2014.11.004.

Karunia J, Niaz A, Mandwie M, et al. (2021). PACAP and VIP modulate LPS-induced microglial activation and trigger distinct phenotypic changes in murine BV2 microglial cells. Int J Mol Sci 22:10947. doi: 10.3390/ijms222010947.

Kularatne RN, Crist RM, Stern ST. (2022). The future of tissue-targeted lipid nanoparticle-mediated nucleic acid delivery. Pharmaceuticals 15:897. doi: 10.3390/ph15070897.

Kuntzel T, Bagnard D. (2022). Manipulating macrophage/microglia polarization to treat glioblastoma or multiple sclerosis. Pharmaceutics 14:344. doi: 10.3390/pharmaceutics14020344.

Laffer B, Bauer D, Wasmuth S, et al. (2019). Loss of IL-10 promotes the differentiation of microglia to a M1 phenotype. Front Cell Neurosci 13:430. [Internet]. Available at: [las accessed 7 Jul 2023] doi: 10.3389/fncel.2019.00430.

Levi G, Minghetti L, Aloisi F. (1998). Regulation of prostanoid synthesis in microglial cells and effects of prostaglandin E2 on microglial functions. Biochimie 80:899–904. Nov doi: 10.1016/s0300-9084(00)88886-0.

Leyh J, Paeschke S, Mages B, et al. (2021). Classification of microglial morphological phenotypes using machine learning. Front Cell Neurosci 15:701673. doi: 10.3389/fncel.2021.701673.

Li C, Ren J, Zhang M, et al. (2022). The heterogeneity of microglial activation and its epigenetic and non-coding RNA regulations in the immunopathogenesis of neurodegenerative diseases. Cell Mol Life Sci 79:511. doi: 10.1007/s00018-022-04536-3.

Liu Y, Zhang R, Yan K, et al. (2014). Mesenchymal stem cells inhibit lipopolysaccharide-induced inflammatory responses of BV2 microglial cells through TSG-6. J Neuroinflammation 11:135. doi: 10.1186/1742-2094-11-135.

Livak KJ, Schmittgen TD. (2001). Analysis of relative gene expression data using real-time quantitative PCR and the 2(-Delta Delta C(T)) Method. Methods 25:402–8. doi: 10.1006/meth.2001.1262.

Martinez A, Hériché J-K, Calvo M, et al. (2023). Characterization of microglia behaviour in healthy and pathological conditions with image analysis tools. Open Biol 13:220200. doi: 10.1098/rsob.220200.

Matsumoto T, Imagama S, Hirano K, et al. (2012). CD44 expression in astrocytes and microglia is associated with ALS progression in a mouse model. Neurosci Lett 520:115–20. doi: 10.1016/j.neulet.2012.05.048.

Medjmedj A, Ngalle-Loth A, Clemençon R, et al. (2022). In cellulo and in vivo comparison of cholesterol, beta-sitosterol and dioleylphosphatidylethanolamine for lipid nanoparticle formulation of mRNA. Nanomaterials (Basel) 12:2446. doi: 10.3390/nano12142446.

Michelucci A, Heurtaux T, Grandbarbe L, et al. (2009). Characterization of the microglial phenotype under specific pro-inflammatory and anti-inflammatory conditions: effects of oligomeric and fibrillar amyloid-β. J Neuroimmunol 210:3–12. doi: 10.1016/j.jneuroim.2009.02.003.

Nadeau S, Rivest S. (1999). Regulation of the gene encoding tumor necrosis factor alpha (TNF-alpha) in the rat brain and pituitary in response in different models of systemic immune challenge. J Neuropathol Exp Neurol 58:61–77. doi: 10.1097/00005072-199901000-00008.

Orihuela R, McPherson CA, Harry GJ. (2016). Microglial M1/M2 polarization and metabolic states. Br J Pharmacol 173:649–65. doi: 10.1111/bph.13139.

Ortiz-Perez A, van TD, R van der M, et al. (2024). Machine learning-guided high throughput nanoparticle design. Digit Discov 3:1280–91. doi: 10.1039/D4DD00104D.

Pan W, Qin M, Zhang G, et al. (2016). Combination of hydrotropic nicotinamide with nanoparticles for enhancing tacrolimus percutaneous delivery. Int J Nanomedicine 11:4037–50. doi: 10.2147/IJN.S108545.

Paolicelli RC, Sierra A, Stevens B, et al. (2022). Microglia states and nomenclature: A field at its crossroads. Neuron 110:3458–83. doi: 10.1016/j.neuron.2022.10.020.

Qin J, Ma Z, Chen X, Shu S. (2023). Microglia activation in central nervous system disorders: A review of recent mechanistic investigations and development efforts. Front Neurol 14:1103416. https://www.frontiersin.org/journals/neurology/articles/10.3389/fneur.2023.1103416/full

Rafiei M, Chung JT, Chau Y. (2023). Roles of biomaterials in modulating the innate immune response in ocular therapy. Front Drug Deliv 3:3. Available at: doi: 10.3389/fddev.2023.1077253.

Reddaway J, Richardson PE, Bevan RJ, et al. (2023). Microglial morphometric analysis: so many options, so little consistency. Front Neuroinform 17:1211188. doi: 10.3389/fninf.2023.1211188.

Riley RS, Kashyap MV, Billingsley MM, et al. (2021). Ionizable lipid nanoparticles for in utero mRNA delivery. Sci Adv 7:eaba1028. doi: 10.1126/sciadv.aba1028.

Roces CB, Lou G, Jain N, et al. (2020). Manufacturing considerations for the development of lipid nanoparticles using microfluidics. Pharmaceutics 12:1095. doi: 10.3390/pharmaceutics12111095.

Rohner E, Yang R, Foo KS, et al. (2022). Unlocking the promise of mRNA therapeutics. Nat Biotechnol 40:1586–600. doi: 10.1038/s41587-022-01491-z.

Saraiva M, O'Garra A. (2010). The regulation of IL-10 production by immune cells. Nat Rev Immunol 10:170–81. doi: 10.1038/nri2711.

Sayers EJ, Peel SE, Schantz A, et al. (2019). Endocytic profiling of cancer cell models reveals critical factors influencing LNP-mediated mRNA delivery and protein expression. Mol Ther 27:1950–62. doi: 10.1016/j.ymthe.2019.07.018.

Shi J, Huang M-W, Lu Z-D, et al. (2022). Delivery of mRNA for regulating functions of immune cells. J Control Release 345:494–511. doi: 10.1016/j.jconrel.2022.03.033.

Shimosakai R, Khalil IA, Kimura S, Harashima H. (2022). mRNA-loaded lipid nanoparticles targeting immune cells in the spleen for use as cancer vaccines. Pharmaceuticals (Basel) 15:1017. doi: 10.3390/ph15081017.

Sun R, Han R, McCornack C, et al. (2023). TREM2 inhibition triggers anti-tumor cell activity of myeloid cells in glioblastoma. Sci Adv 9:eade3559. doi: 10.1126/sciadv.ade3559.

Swart LE, Koekman CA, Seinen CW, et al. (2022). A robust post-insertion method for the preparation of targeted siRNA LNPs. Int J Pharm 620:121741. doi: 10.1016/j.ijpharm.2022.121741.

Takahashi K, Yamamoto K, Kuchiba A, et al. (2023). Hypothesis testing procedure for binary and multi-class F1-scores in the paired design. Stat Med 42:4177–92. doi: 10.1002/sim.9853.

Tanaka H, Miyama R, Sakurai Y, et al. (2021). Improvement of mRNA delivery efficiency to a T cell line by modulating PEG-lipid content and phospholipid components of lipid nanoparticles. Pharmaceutics 13:2097. doi: 10.3390/pharmaceutics13122097.

Tang X, Zhang Y, Han X. (2023). Ionizable lipid nanoparticles for mRNA delivery. Adv NanoBiomed Res 3:2300006.

Veiga N, Goldsmith M, Granot Y, et al. (2018). Cell specific delivery of modified mRNA expressing therapeutic proteins to leukocytes. Nat Commun 9:4493. doi: 10.1038/s41467-018-06936-1.

Wang SK, Cepko CL. (2022). Targeting microglia to treat degenerative eye diseases. Front Immunol 13:843558. doi: 10.3389/fimmu.2022.843558.

Wang X, Liu S, Sun Y, et al. (2023). Preparation of selective organ-targeting (SORT) lipid nanoparticles (LNPs) using multiple technical methods for tissue-specific mRNA delivery. Nat Protoc 18:265–91. doi: 10.1038/s41596-022-00755-x.

Wang L, Liu Q, Zhang Y, et al. (2019). Establishment of BV2 microglia polarization model and its effect on Toxoplasma gondii proliferation. Res Vet Sci 125:382–9. doi: 10.1016/j.rvsc.2019.08.002.

Wang Y, Yu P, Li Y, et al. (2021). Early-released interleukin-10 significantly inhibits lipopolysaccharide-elicited neuroinflammation in vitro. Cells 10:2173. doi: 10.3390/cells10092173.

Xia Y, Wu Q, Mak S, et al. (2022). Regulation of acetylcholinesterase during the lipopolysaccharide-induced inflammatory responses in microglial cells. Faseb J 36:e22189. doi: 10.1096/fj.202101302RR.

Xiao H, Han S, Baigude H. (2021). Regulation of microglia polarization via mannose receptor-mediated delivery of siRNA by ligand-functionalized DoGo LNP. RSC Adv 11:32549–58. doi: 10.1039/d1ra04293a.

Xue M, Gao D, Chen X, et al. (2011). New dimeric cholesteryl-based A(LS)2 gelators with remarkable gelling abilities: organogel formation at room temperature. J Colloid Interface Sci 361:556–64. doi: 10.1016/j.jcis.2011.05.074.

Yamankurt G, Berns EJ, Xue A, et al. (2019). Exploration of the nanomedicine-design space with high-throughput screening and machine learning. Nat Biomed Eng 3:318–27. doi: 10.1038/s41551-019-0351-1.

Yan DM, Zhang YM, Ji YH, et al. (2021). Re-visit the concept of M1 versus M2 phenotypes of BV2 microglia and test their effects on stroke outcome in mice. Cardiol Plus 6:264–73. Octdoi: 10.4103/2470-7511.334399.

Yavuz A, Coiffier C, Garapon C, et al. (2023). DLin-MC3-containing mRNA lipid nanoparticles induce an antibody Th2-biased immune response polarization in a delivery route-dependent manner in mice. Pharmaceutics 15:1009. doi: 10.3390/pharmaceutics15031009.

Young RE, Nelson KM, Hofbauer SI, et al. (2024). Systematic development of ionizable lipid nanoparticles for placental mRNA delivery using a design of experiments approach. Bioact Mater 34:125–37. doi: 10.1016/j.bioactmat.2023.11.014.

Zhang H, Han X, Alameh M-G, et al. (2022). Rational design of anti-inflammatory lipid nanoparticles for mRNA delivery. J Biomed Mater Res A 110:1101–8. doi: 10.1002/jbm.a.37356.

Zhao N, Francis NL, Calvelli HR, Moghe PV. (2020). Microglia-targeting nanotherapeutics for neurodegenerative diseases. APL Bioeng 4:030902.

Zhu Y, Ma J, Shen R, et al. (2024). Screening for lipid nanoparticles that modulate the immune activity of helper T cells towards enhanced antitumour activity. Nat Biomed Eng 8:544–60. doi: 10.1038/s41551-023-01131-0.